High Resolution Fourier Transform Infrared Spectroscopy of the Quantum Magnet $LiTmF_4$

July 2018

Master Thesis
Institute of Physics

Benoit Truc

Supervised by Prof. Henrik Rønnow and Dr. Peter Babkevich
Laboratory for Quantum Magnetism

Contents

Introduction

In fundamental interactions research, dipolar magnets are particularly interesting to study since they provide a large spectrum of quantum phenomena [1-2]. Magnetic dipolar interaction are omnipresent in magnetic systems. However, in most of materials, various exchange interactions within the crystal environment hide the purely dipolar interaction.

It has been shown [2-3] that in LiRF$_4$ family, where R is a rare earth element the exchange interactions with nearest neighbours can be neglected. Moreover, by simply changing the R ion in the tetrafluoride lithium matrix, the magnetic behaviour can completely differ at low temperature. For instance LiHoF$_4$ is a Ising ferromagnet [4], while LiErF$_4$ is a XY antiferromagnet [5] and LiTmF$_4$ a Van Vleck paramagnet [6]. In order to understand theses systems, a detailed comprehension of the electronic crystal field is necessary, since the ground state is determined by this interaction [7]. The energy range corresponds typically to the infrared region. While a lot of studies have been done in other LiRF$_4$, LiTmF$_4$ has not be fully investigated.

This work presents the spectroscopy analysis from the far to the near infrared regions ($10 - 10'000\,\mathrm{cm}^{-1}$) of a pure LiTmF$_4$ single crystal at cryogenic temperatures using Fourier Transform Spectroscopy technique.

The first part details the structure and the energy scale. The experimental details and FTIR spectroscopy will be then presented. The third chapter is dedicated to explain how the energy levels have been assigned and their strength. The results for the first three manifolds are presented and exhibit some intriguing results such as splitting. Finally, one will discuss the perspectives.

1 The Quantum Magnet $LiTmF_4$

The $LiTmF_4$ is an insulating Van Vleck paramagnet and exhibits a giant magnetostriction [8]. Thulium is one of the heaviest rare element and its ion Tm^{3+} has a $4f^{12}$ electronic configuration which gives 91 degenerate states. The ground state configuration is given by Hund's rules and is represented in Fig.1.1(c). Tm element has a non zero nuclear spin which can give rise to hyperfine splitting.

The degeneracy of the 91 energy levels is lifted by the Spin-Orbit coupling depending on the electronic configuration plus the crystal field interaction representing the electrostatic repulsion and orbital hybridization between the surrounding ions. The purpose of this work consists to analyse this lifting. The electronic ground state configuration of last rare earth elements are given in Table 1.1.

R^{3+}	Shell	Term	S	L	J	I
Gd	$4f^7$	$^8S_{7/2}$	7/2	0	7/2	3/2
Tb	$4f^8$	$^7F_6$	3	3	6	3/2
Dy	$4f^9$	$^6H_{15/2}$	5/2	5	15/2	5/2
Ho	$4f^{10}$	$^5I_8$	2	6	8	7/2
Er	$4f^{11}$	$^4I_{15/2}$	3/2	6	15/2	7/2
Tm	$4f^{12}$	$^3H_6$	1	5	6	1/2
Yb	$4f^{13}$	$^2F_{7/2}$	1/2	3	7/2	1/2*

Table 1.1 – Electronic ground state structure given by the Hund's rules of the heavier $4f$ elements, where S is the spin momentum, L the angular momentum, J the total momentum and I is the nuclear spin.
* ^{173}Yb isotope has a nuclear spin = 5/2.

1.1 Crystal Structure

The LiRF$_4$ compounds belongs to the family of Scheelite crystal structure, where R is the Rare earth ion. Its structure shown in the Fig.1.1(a) and (b) taken from [7] is in the $I4_1/a$ space group. The rare earth ion has a point-symmetry group S_4 yielding to a term reduction of the crystal field Hamiltonian discussed in the next section.

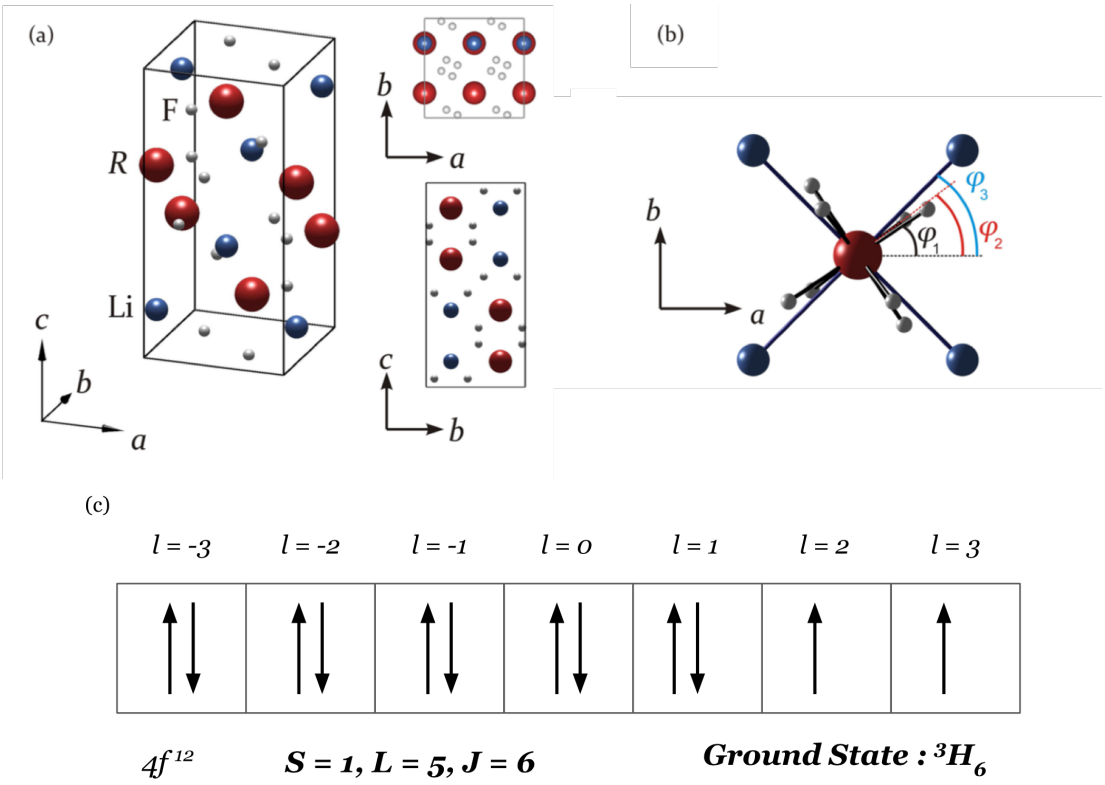

Figure 1.1 – (a) Scheelite tetragonal crystal structure of LiRF$_4$ compound, with a $S_4(4/m)$ point group symmetry, lattice constants are approximately $a = b \simeq 5.2\,\text{Å}$ and $c \simeq 10.5\,\text{Å}$. (b) In the ab plane the ions have an angle of $\varphi_1 = 34$ř, $\varphi_2 = 37$ř, $\varphi_3 = 45$ř from the a-axis. (c) Ground state representation of the $4f^{12}$ electrons configuration given by Hund's rules.

According to the $S_4(\bar{4})$ point group symmetry of the ion, there are three irreducible representation, Γ_1, Γ_2 unidimensional and Γ_{34} of dimension two, where the same notation convention used in [9] is followed. The Table 1.2 give the number of each irreducible representation depending on the total angular momentum and the crystal symmetry.

	S_4 symmetry		
J	Γ_1	Γ_2	Γ_{34}
7	3	4	4
6	3	4	3
5	3	2	3
4	3	2	2
3	1	2	3

Table 1.2 – Number of states with its irreducible representation depending of the total angular momentum for the S_4 point group symmetry.

1.2 Energy Scales

In this work, we are interested to the identification and characterization of the $LiTmF_4$ energy levels splitted by the interactions with its crystal environment and the electronic configuration. Since no significant external magnetic or electric field were applied during the experiment and the interaction exchange can be neglected in this compound, the effective single-ion Hamiltonian $\mathcal{H}$ is given by

$$\mathcal{H} = \mathcal{H}_{CF} + \mathcal{H}_{SO} \tag{1.1}$$

where the first term is the crystal-field Hamiltonian and the last term is the Spin-Orbit coupling. Although thulium have a nonzero nuclear spin, the hyperfine interaction would not be considered in the model. The Spin-Orbit interaction is given by the usual relation

$$\mathcal{H}_{SO} = \zeta \sum_i \mathbf{L}_i \cdot \mathbf{S}_i \tag{1.2}$$

where ζ is the atomic spin-orbit coupling, $\mathbf{L}$ the angular momentum and $\mathbf{S}$ the spin of each ion.

The crystal-field (CF) Hamiltonian describes the interaction between the rare earth ion and its surrounding Li^+ and F^- ions. The general form is given by

$$\mathcal{H}_{CF} = \sum_i \sum_{l,m} B_l^m \hat{O}_l^m(\mathbf{J}_i) \tag{1.3}$$

where the first summation goes over all ions and $\hat{O}_l^m$ are the Stevens' Operators with B_l^m as coefficients and $\mathbf{J_i}$ the total angular momentum. The CF Hamiltonian is defined by the environment surrounding the R ion. Since the local point group symmetry of the R ion is $S_4(4/m)$, the nonzero B_l^m coefficients are constrained to have $m = 0, \pm 4$

$$\mathcal{H}_{CF} = \sum_{l=2,4,6} B_l^0 \hat{O}_l^0(\mathbf{J}) + \sum_{l=4,6} B_l^4(c)\hat{O}_l^4(c)(\mathbf{J}) + B_l^4(s)\hat{O}_l^4(s)(\mathbf{J}) \tag{1.4}$$

where by convention and for $m \neq 0$

$$\hat{O}_l^m(c) = \frac{1}{\sqrt{2}}\left[\hat{O}_l^{-m} + (-1)^m \hat{O}_l^m\right], \tag{1.5}$$

$$\hat{O}_l^m(s) = \frac{i}{\sqrt{2}}\left[\hat{O}_l^{-m} - (-1)^m \hat{O}_l^m\right]. \tag{1.6}$$

By rotating the basis described in [7], one can vanish the $B_4^4(s)$ term so as B_4^4 is real.

For the first manifold, the CF Hamiltonian is given by

$$\mathcal{H}_{CF} = B_2^0\hat{O}_2^0(\mathbf{J}) + \Big[B_4^0\hat{O}_4^0(\mathbf{J}) + B_4^4(c)\hat{O}_4^4(c)(\mathbf{J})\Big] + \Big[B_6^0\hat{O}_6^0(\mathbf{J}) + B_6^4(c)\hat{O}_6^4(c)(\mathbf{J}) + B_6^4(s)\hat{O}_6^4(s)(\mathbf{J})\Big]. \quad (1.7)$$

It can be shown [9] that the CF Hamiltonian can be extended to higher energy levels. The Fig.1.2 obtained by a numerical calculation illustrates the lifting of the degeneracy due to the Spin-Orbit coupling and the crystal field interaction. The first excited manifold is around 8'200 K above the ground state, while the difference energy of the ground state and the first excited energy level is approximately 40 K. The Table 1.3 gives the formulation of the Stevens Operators considered.

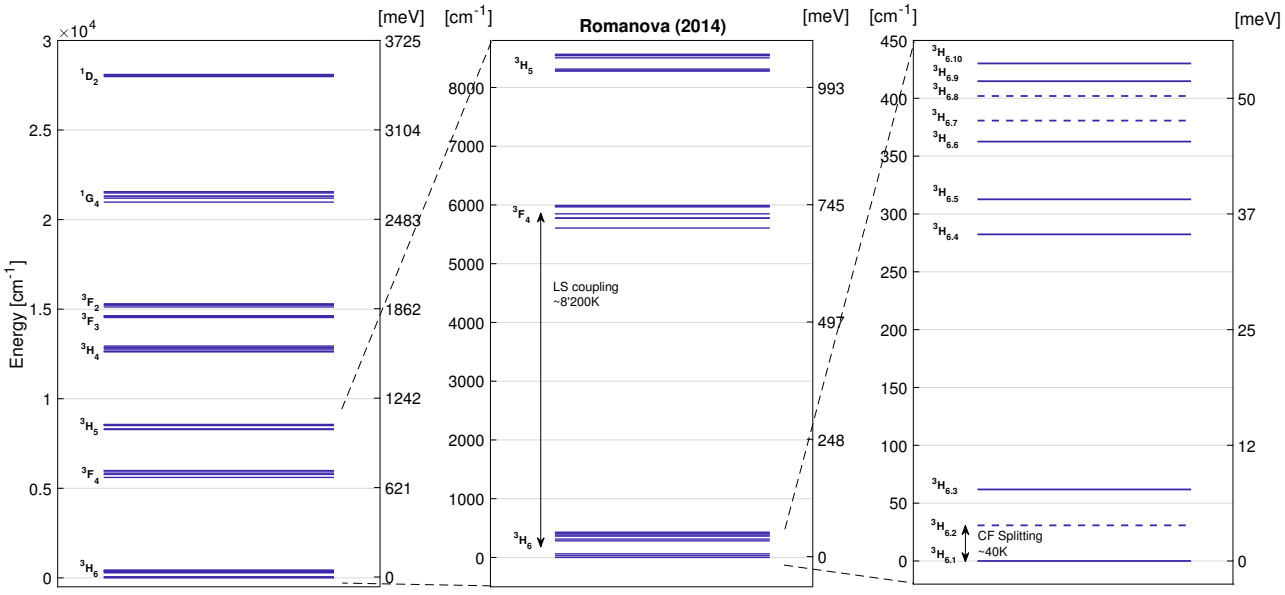

Figure 1.2 – Calculated energy levels of the $LiTmF_4$ using the *spectre* software and the CF parameters from Romanova (2014) [10]. Left : eight first manifolds, middle : example of LS splitting, right : further splitting in ground manifold due to the crystal field, the dashed line represents a doubly degenerate state.

$\hat{O}_2^0$	=	$[3\hat{J}_z^2 - X]$
$\hat{O}_4^0$	=	$[35\hat{J}_z^4 - (30X - 25)\hat{J}_z^2 + (3X^2 - 6X)]$
$\hat{O}_4^4$	=	$\frac{1}{2}[\hat{J}_+^4 + \hat{J}_-^4]$
$\hat{O}_6^0$	=	$[231\hat{J}_z^6 - (315X - 735)\hat{J}_z^4 + (105X^5 - 525X + 294)\hat{J}_z^2 - 5X^3 + 40X^2 - 60X]$
$\hat{O}_6^4(c)$	=	$\frac{1}{4}[(11\hat{J}_z^2 - X - 38)(\hat{J}_+^4 + \hat{J}_-^4) + (\hat{J}_+^4 + \hat{J}_-^4)(11\hat{J}_z^2 - X - 38)]$
$\hat{O}_6^4(s)$	=	$\frac{1}{4i}[(11\hat{J}_z^2 - X - 38)(\hat{J}_+^4 + \hat{J}_-^4) + (\hat{J}_+^4 + \hat{J}_-^4)(11\hat{J}_z^2 - X - 38)]$

Table 1.3 – Expression of the Stevens Operators, $X = J(J+1)$ and $\hat{J}_\pm = \hat{J}_x \pm i\hat{J}_y$.

1.2.1 Numerical Calculation

In order to compare the experimental results obtained by FTIR spectroscopy presented further with theoretical expectations, one has used the *spectre* software provide by the university of Oxford[1] which allows us to calculate the energy levels.

The software assumes a f^n configuration which means that the n f-electrons are equivalent. The same Hamiltonian as in eq(1.1) is considered. Additional terms like the Zeeman interaction or an exchange field energy could be included. However, theses terms are set to zero in our case, since none external magnetic field has been applied and the exchange interaction can be neglected.

Electronic and spin-orbit parameters in the free ion Hamiltonian is already implemented and are taken from [11]. A list of the free parameters B_l^m found in previous works is summarized in Table 1.4.

The first 68 energy levels and the first excited manifold $^3F_4$are plotted in Fig.1.3. Although the CF parameters varies from one article to another, global locations of the manifolds are very similar. It is expected since, this forbidden region is related to the Spin-Orbit interaction and not to Crystal Field Splitting. The $^3F_4$ manifold shows the variation between the parameters. Note the doubly degenerate state is always at second and last energy levels of the manifold.

B_2^0	B_4^0	B_4^4	B_6^0	$B_6^4(c)$	$B_6^4(s)$	Ref.
45.56	-88.89	113.97	-7.95	76.35	14.65	[12]
45.69	-89.02	114.10	-8.07	76.85	0	[12]
44.53	-75.46	104.81	-21.48	78.12	0	[13]
42.80	-79.58	107.08	-18.90	77.82	0	[13]
43.21	-79.33	-107.27	-22.60	-79.58	0	[14]
45.69	-89.39	-104.94	-8.06	-76.80	-0.006	[6]
45.69	-89.39	-109.74	-8.06	-77.92	2.41	[10]

Table 1.4 – Crystal Field parameters of $LiTmF_4$ in meV used for the energy levels calculation using *spectre* software.

[1] https://groups.physics.ox.ac.uk/Boothroyd/software.htm

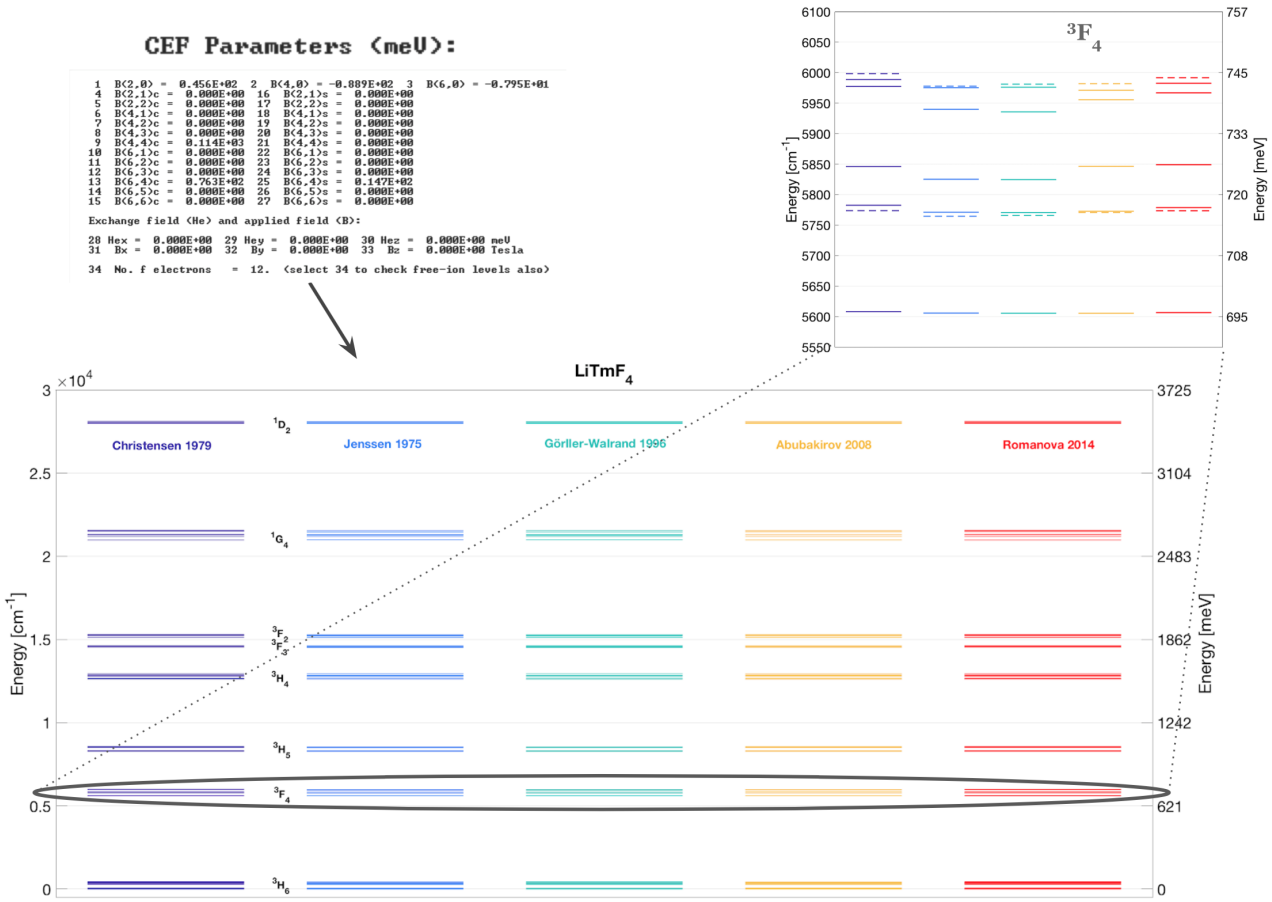

Figure 1.3 – Numerical calculation of the $LiTmF_4$ energy levels using the CF parameters in Table 1.4

2 Experimental Details

In this chapter, one covers how the energy spectrum of the sample is obtained. In particular, the technique of the Fourier Transform Infrared Spectroscopy (FTIR) is presented. The experimental conditions of the experiment are also discussed.

2.1 Principle of Fourier Transform Infrared Spectroscopy

The interest for Fourier Transform Infrared Spectroscopy has growth this last decades since it can provide a spectrum with a drastic higher resolution than common grating spectrometers with a much faster time acquisition. Unlike dispersive spectrometers, FTIR spectroscopy uses a broad spectrum including all the frequencies which drastically increases the throughput and sampling time. However, FTIR techniques give an interferogram and an extra step is needed to retrieved the spectrum. This additional step is the computation of the Fourier transform of the interferogram giving the name to the method. The following sections describe operations and essential components of FTIR spectroscopy. More details about that technique can be found in the following references [15–17].

2.1.1 Interferogram and Spectrum

The heart of Fourier transform spectrometer is an interferometer. The Michelson Interferometer is usually preferred because of its simplicity.

A bright polychromatic light is introduced in the interferometer. The incident light is splitted by a beam splitter in two equivalent beams. One is reflected by a fixed mirror while the second is reflected by a movable mirror which modify the optical path length. They recombine and interfere *i.e.* modify the incident spectrum at the beam splitter. Indeed for each step of the movable mirror one wavelength vanishes because of destructive interferences. Then the light passes through and interacts with the sample. The transmission signal depending on the movable mirror is finally recorded by a photo-detector. A sketch of a FITR spectrometer using Michelson interferometer is depicted on the Fig.2.3

For a polychromatic white light, Chamberlain (1979) has shown [18] for a wavenumber-dependent intensity function $I(\tilde{\nu})$ the interference signal $I^{\text{interf}}(x)$ is given by

$$I^{\text{interf}}(x) = \int_0^\infty I(\tilde{\nu})\mathrm{d}\tilde{\nu} + \int_0^\infty I(\tilde{\nu})\cos(2\pi\tilde{\nu}x)\mathrm{d}\tilde{\nu} \qquad (2.1)$$

where x is the position of the movable mirror and the integration goes over all the wavenumbers $\tilde{\nu}$. We call *zero-path-difference* the case $x = 0$, *i.e.* when the optical path difference is zero. It gives rise to constructive interferences, one has

$$I^{\text{interf}}(x = 0) = 2\int_0^\infty I(\tilde{\nu})\mathrm{d}\tilde{\nu}. \qquad (2.2)$$

Combining eq.(2.1) and eq.(2.2), one obtains

$$I^{\text{interf}}(x) = \frac{1}{2}I^{\text{interf}}(0) + \overbrace{\int_0^\infty I(\tilde{\nu})\cos(2\pi\tilde{\nu}x)\mathrm{d}\tilde{\nu}}^{interferogram\, F(x)}. \qquad (2.3)$$

The second term corresponds to the *interferogram* $F(x)$ which depends on the position of the movable mirror. By taking the Fourier transform of the interferogram, we finally obtain the spectral distribution wavenumber-dependent

$$I(\tilde{\nu}) = C\int_0^\infty F(x)\cos(2\pi\tilde{\nu}x)\mathrm{d}x \qquad (2.4)$$

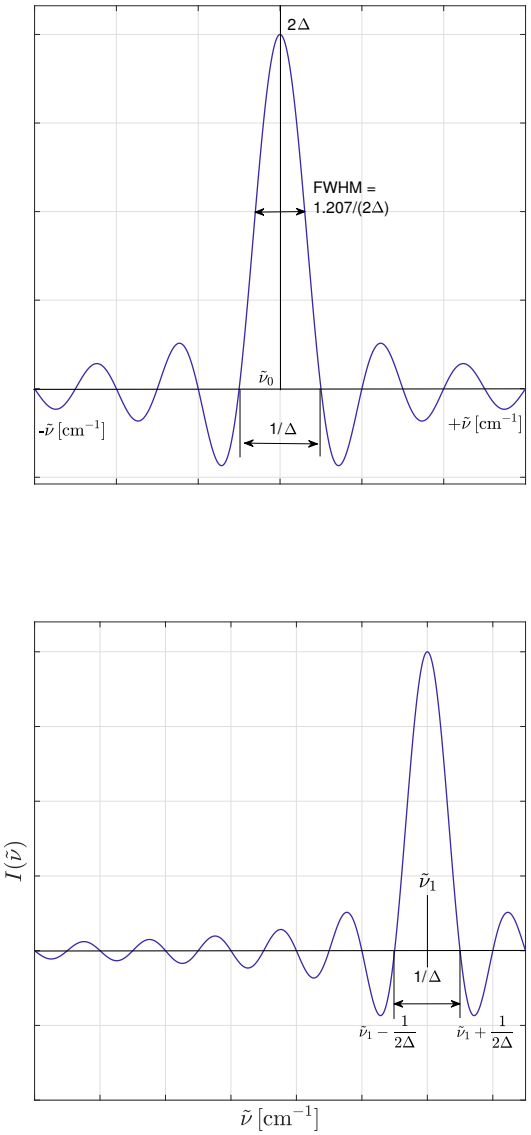

Figure 2.1 – top : Fourier transform of a boxcar truncation function with a cardinal sine function shape. Bottom : Fourier transform of sinusoidal interferogram at wavenumber $\tilde{\nu}_1$ for a monochromatic signal with Δ retardation.

with C as a normalization constant. The eq.(2.4) shows that theoretically the entire spectrum can be deduced (from 0 to $+\infty\,\text{cm}^{-1}$) with an infinitely high resolution. However, in practice, the resolution is finite since the distance x of the movable mirror is finite. If the maximum optical path difference *i.e.* retardation is restricted to Δ in centimeters ($x_{\max}$ in Michelson interferometer sketch Fig.2.3), the spectral distribution is then multiplied by a *boxcar truncation function* $D(x)$. The *unapodized resolution* $\Delta\tilde{\nu}$ is linked by $\Delta\tilde{\nu} \simeq 0.6\Delta$. In this project a Bruker instrument was used with $\Delta = 11.7\,\text{m}$ and has a theoretical resolution $\Delta\tilde{\nu} = 0.00053\,\text{cm}^{-1}/0.066\,\mu\text{eV}$ while precision of the absorption peak center is directly related to the precision of the movable mirror.

$D(x)$ is defined by

$$D(x) = \begin{cases} 1 & \text{if} \quad -\Delta \leq x \leq \Delta \\ 0 & \text{else} \end{cases} \tag{2.5}$$

which gives an effective intensity

$$I_{\text{eff}}(\tilde{\nu}) = C \int_0^{\infty} F(x) D(x) \cos(2\pi\tilde{\nu}x) \mathrm{d}x. \tag{2.6}$$

Since the Fourier transform of the product of two functions is equal to the convolution of the Fourier transform of each function, the eq.(2.6) can be written as

$$I_{\text{eff}}(\tilde{\nu}) = I(\tilde{\nu}) * S_I(\tilde{\nu}) \tag{2.7}$$

where S_I is the instrumental line function resulting from the Fourier transform of $D(x)$ expressed by

$$S_I(\tilde{\nu}) = 2\Delta \frac{\sin(2\pi\tilde{\nu}\Delta)}{2\pi\tilde{\nu}\Delta} \equiv 2\Delta \, sinc(2\tilde{\nu}\Delta). \tag{2.8}$$

The Fig.2.1 illustrates the eq.(2.8) and its consequences for the Fourier transform of a monochromatic light.

In addition, the aperture has a finite size d and creates circular fringes which leads to the multiplication of the interferogram envelope by a *sinc* function, this effect is called *self-apodization*. An optimum size aperture can be found in order to maximize the fringe amplitude for the largest measurable wavenumber $\tilde{\nu}_{max}$ given by [19]

$$d = \sqrt{\frac{4f^2}{\Delta\tilde{\nu}_{max}}} \tag{2.9}$$

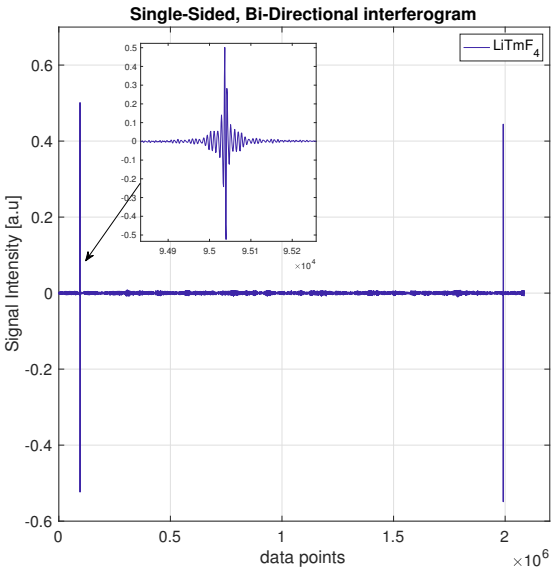

(a) Interferogram

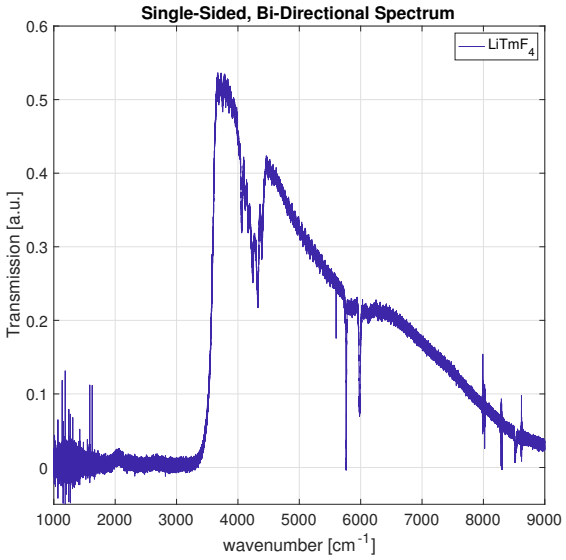

(b) associated spectrum

Figure 2.2 – Temperature=5 K, Detector=InSb, BS=CaF_2, polarization=//, resolution=0.03 cm^{-1}, aperture=1.7 mm

with f the focal distance of the parabolic mirror ($f = 41.8$ cm in this work).

The effect of having a finite size aperture has to be considered in $S_I(\tilde{\nu})$.

For a peak position $\tilde{\nu}_0$ the relation becomes

$$S_{\mathrm{I}}(\tilde{\nu}) \simeq \overbrace{\left[\Omega_{max}\frac{2\pi}{\tilde{\nu}_0\Omega_{max}}\Pi\left(\frac{2\pi\tilde{\nu}}{\tilde{\nu}_0\Omega_{max}}\right)\right]}^{\text{finite aperture size}} \quad * \quad \overbrace{2\Delta\ sinc(2\tilde{\nu}\Delta)}^{\text{finite path difference}} \tag{2.10}$$

with $\Omega_{max} = \frac{\pi}{\Delta\tilde{\nu}_{max}}$ the considered solid angle.

In eq.(2.6), one has used the truncation function $D(x)$ which leads to a convolution of the true spectrum with a *sinc* function. Two case can appear, if the width of true absorption is large compare to the width of the instrumental *sinc* function, the effect of its oscillatory behaviour is limited. On the contrary, the side lobes affect the true spectrum. To reduce this artefact, one uses *apodization*[1] functions. The chosen apodization function depend on the absorption peak features and the instrumental limitations. Finally, the eq.(2.6) can be written in a general form of

$$I_{\text{eff}}(\tilde{\nu}) = C\int_0^\infty F(x)W(x)\cos(2\pi\tilde{\nu}x)\mathrm{d}x \tag{2.11}$$

with $W(x)$ a weighting function, called *apodization* function. There is always a trade off between resolution and the amplitude oscillation which will depend on each specific configuration. For this work the selected apodization function is the Blackman-Harris 3-terms.

The ZPD corresponding to the movable mirror position where maximum interference occur can be placed close to the beginning or in the middle of the interferogram. The interferogram is called respectively *Single-Sided* and *Double-Sided*. One can collect data in both movable mirror direction, if so the *bi-directional* term is added. The two measures are usually combined with the forward scan in the first half and the backward-direction in the second half of the interferogram. In this configuration, the two measures have to be performed independently, since the interferogram are not in phase and need a different phase correction. One then recombines the result by averaging. A phase correction has to be applied since the interferogram can contain out-of-phase elements caused by different optical paths.

An example of a Single-Sided Bi-Directional interferogram is presented on the Fig.2.2(a). The data points correspond to each measure at a given position with a fixed step size and are characteristic to the spectrometer used. By performing the Fourier transform with the Blackman-Harris 3-terms as apodization function and a phase correction using Mertz [20] method, the spectrum wavenumber-dependent is obtained on the Fig.2.2(b).

2.1.2 Advantages

The resolution limitation is only determined by the maximal optical path distance. In general, FTIR spectrometer provide a much better resolution than dispersive instruments.

[1] from Greek literally meaning "removing the feet"

Fellgett Advantage

One main advantage of the Fourier Transform Spectroscopy is the ability to take multiplexed measurements instead of direct measures in dispersive methods. One consequence is for one single measure the signal-to-noise (SNR) ration is greater by a factor of $\sqrt{m}$, where m is the number of sample points within the desired spectrum. Furthermore, one measure can be taken in identical conditions, while in dispersive instrument there is grating, or one has to change the filter.

Jacquinot Advantage

Unlike dispersive methods which need slits to properly collimate the beam, in FTIR instruments the energy throughput is higher. In combination with the Fellgett advantage, FTIR measurement take a much shorter time with a better SNR.

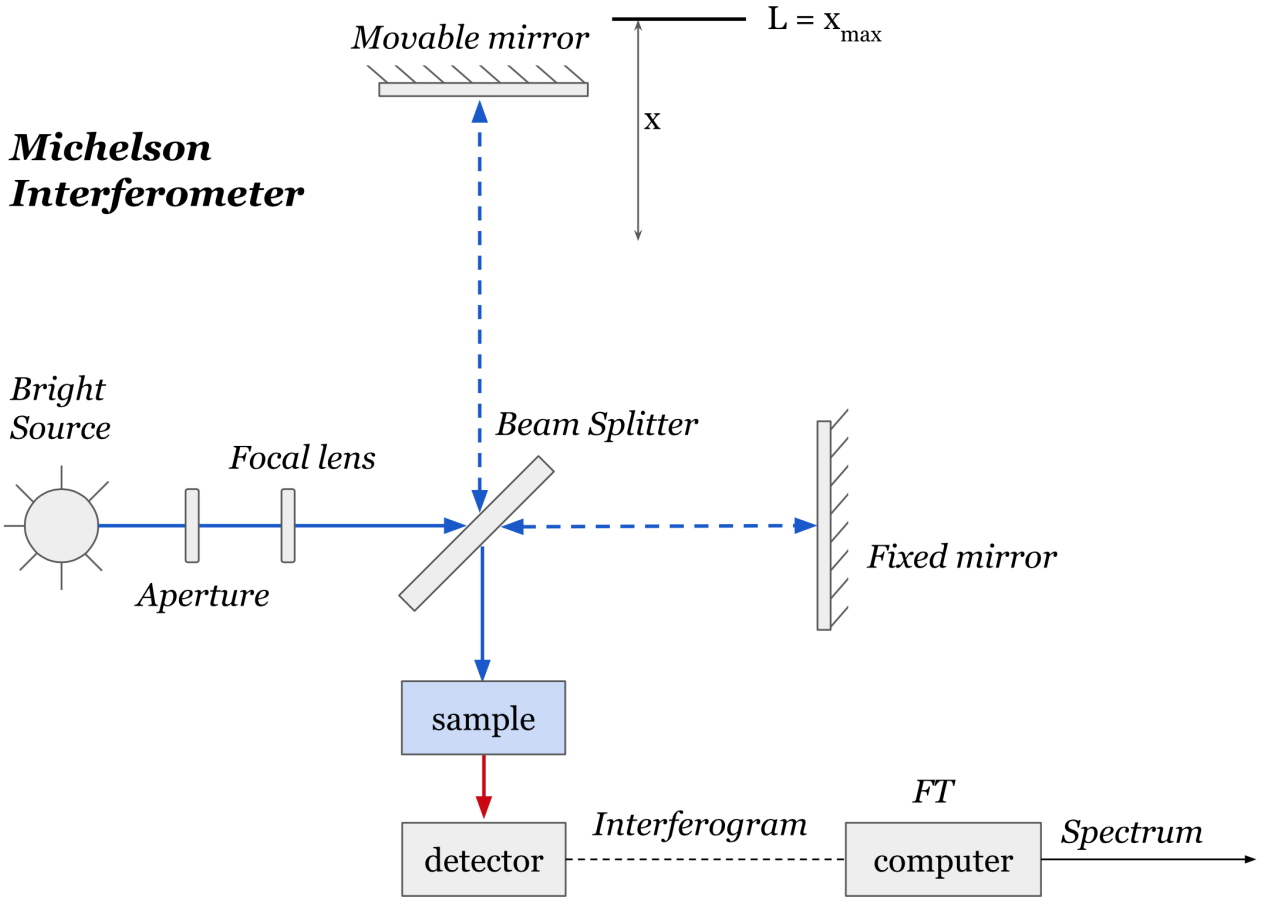

Figure 2.3 – (a) Sketch of a Michelson interferometer used for Fourier Transform Spectroscopy. A bright light from a polychromatic source is splitted by the Beam Splitter. One beam is reflected by a fixed mirror while the second is reflected by a movable mirror which modifies the optical distance. They recombine and pass through the sample. Finally the spectrum is retrieved by computing the Fourier Transform (FT) of the obtained interferogram.

2.1.3 Detectors

Several detectors are used depending the energy range we are interested in. The Fig.2.4 illustrates the efficiency of different detectors. Three detectors are installed.

For the far-infrared region (FIR) $30 - 400\,\mathrm{cm}^{-1}$ a Bolometer cooled with liquid helium is used. An additional filter in front of the detector is applied to cut off the higher energies.

The mid-infrared region (MIR) $4'000 - 10'000\,\mathrm{cm}^{-1}$ has been investigated using a Indium Antimonide (InSb) photo-detector cooled with liquid nitrogen. A Mercury Cadmium Telluride (MCT) is also available, but was not useful for our measurements.

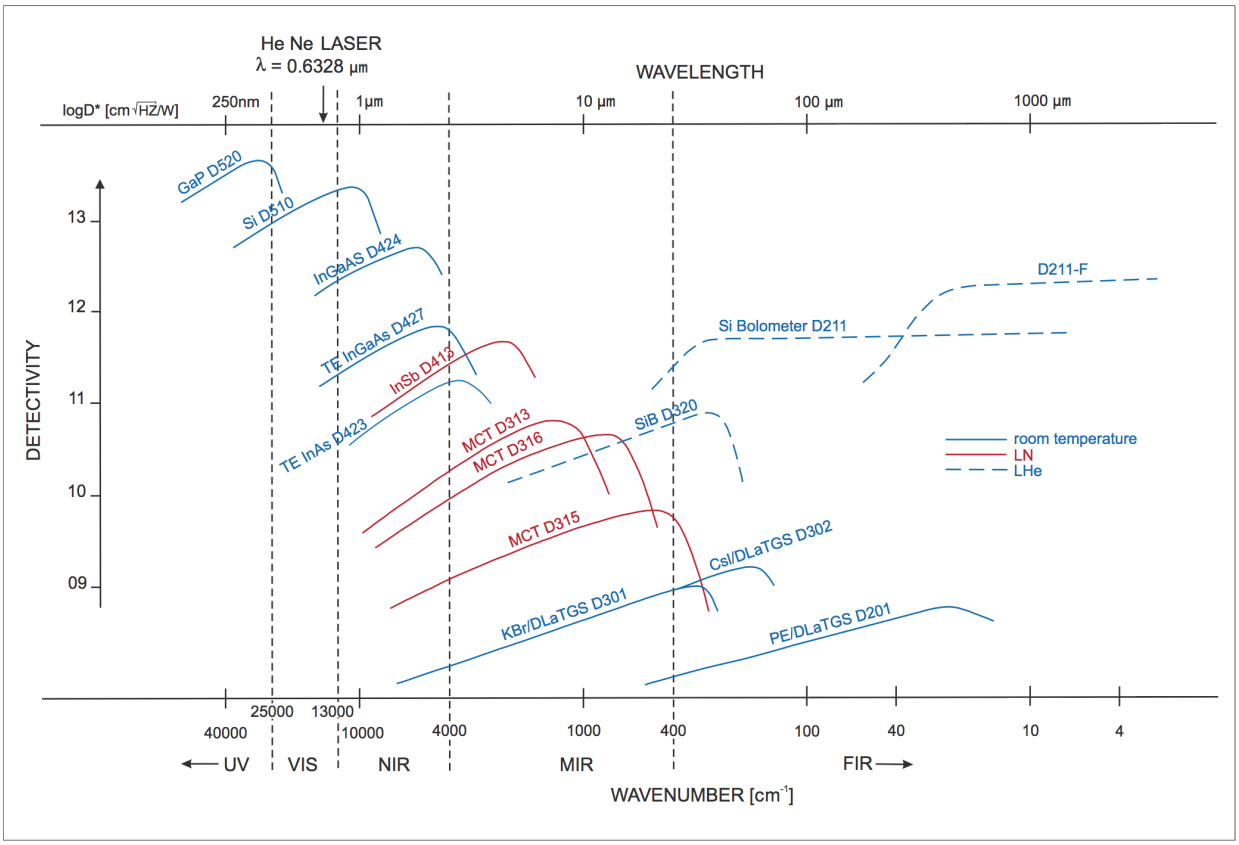

Valid for FT-IR spectrometers

Figure 2.4 – Detectivity for several detectors depending on the wavelength. The InSb D413 and the Si Bolometer D211 have been used for this experiment, graphic taken from [21]

2.1.4 Beam Splitters

Different Beam Splitters (BS) are used depending on the region scanned. Indeed the efficiency of the BS depends on the wavelength. In our setup, for the far-infrared a 23 μm Mylar beam splitter is mounted, while in the mid-infrared a 3.5 μm Mylar or a calcium fluoride (CaF_2) beam splitter are used. The Fig.2.5 shows the working region for several beam splitter.

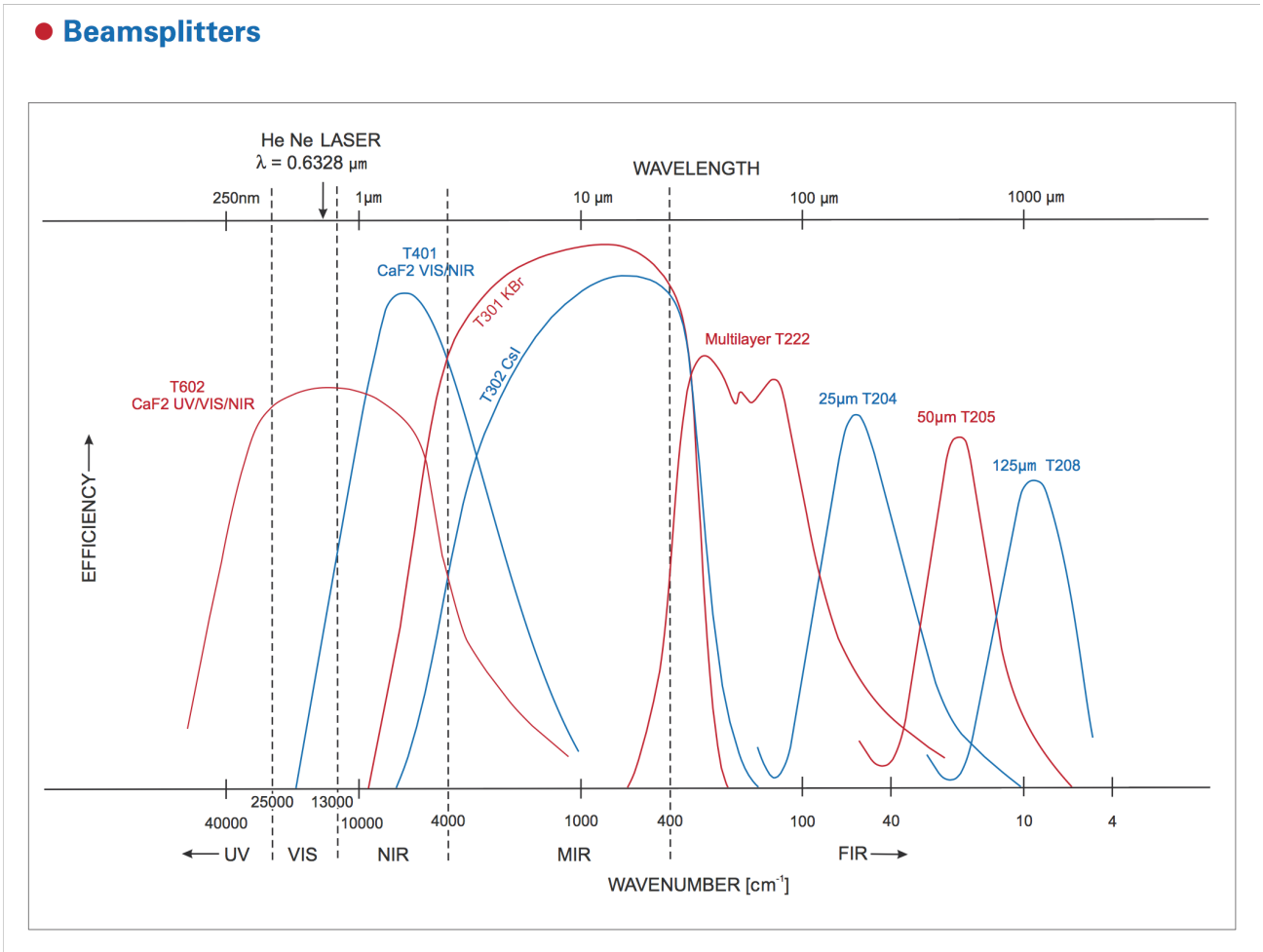

Figure 2.5 – Strong dependence between the Beam Splitter efficiency and the photon energy. A Calcium Fluoride, a 23 μm and a 3.5 μm Mylar have been used, graphic taken from [21]

2.1.5 Sources

Several sources can be used and provide different brightness and spectrum. To name only a few, for the NIR region a tungsten-halogen lamp is commonly used since it can reach high temperature and therefore radiates a broad spectrum. A light from a heated silicon carbide compound is appropriate for the MIR while a mercury-vapor discharge lamp can be used for the far IR. Finally, synchrotron light source presents several advantages since it provide a bright, polarized light and a broad spectrum.

2.2 Experimental Setup

The optical spectroscopic features of the pure $LiTmF_4$ single crystal have been obtained by using a Bruker IFS 125HR high-resolution FT-IR Fig.2.6(a) under vacuum with a theoretical unapodized resolution of $0.00053\,cm^{-1}/0.066\,\mu eV$ where the maximum optical path distance of the instrument is 11.7 m. The spectrometer is linked with the third-generation Synchroton light source of the Paul Scherrer Institute, the Swiss Light Source with an electron beam energy of 2.4 GeV. The light emitted by the source is highly linearly polarized >99.999% therefore is very suitable for polarization analysis.

The $LiTmF_4$ single crystal of $120\mu m$ thickness has been growth by AC materials is mounted within the cryostat using silver paint to ensure the cooling, presented in Fig.2.6(b). The c-axis of the sample found by Laue diffraction can be adjusted to be parallel or perpendicular with the incident beam. We will use thereafter the notation x and z polarization to refer as perpendicular and parallel polarization respectively. The cryostat is then placed in a vacuum chamber (red circle) with a working pressure around 10^{-7} mbar. An Oxford Instrument in combination with a liquid helium cooling system and a heater control the desired temperature from 3.6K to room temperature.

Three different detectors can be used depending on the energy region scanned as discussed in **chapter 4** and are shown in Fig.2.6(c).

The optical settings (size aperture and resolution) and data record is done by the Bruker software *Opus* which also computes the spectrum. The obtained spectrum is finally analysed by a home made Matlab code.

(a)

(b)

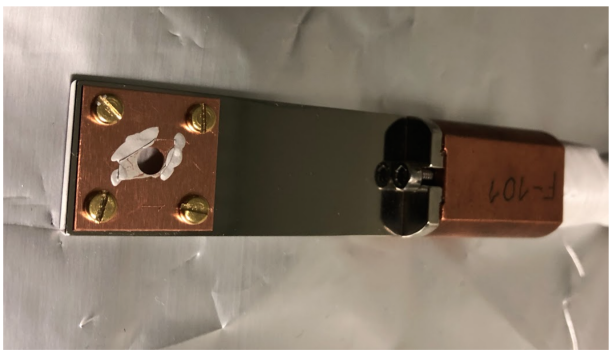

(c)

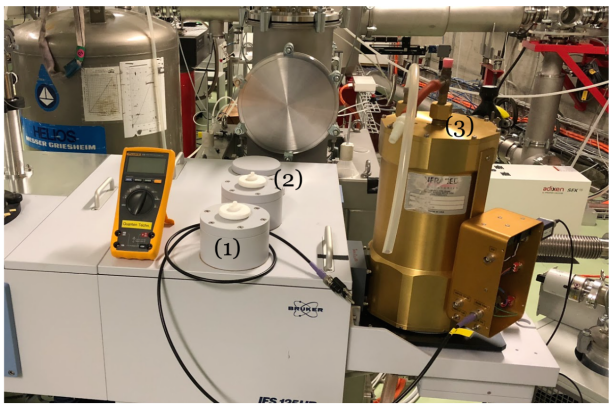

Figure 2.6 – (a) The Bruker IFS 125HR high-resolution FT-IR with its two arms. Inside the red circle the cryostat chamber. (b) the transparent $LiTmF_4$ sample glue with silver paint (c) Three photo-detectors (1) Mercury Cadmium Telluride (MCT), (2) Indium Antimonide (InSb) and (3) the Bolometer.

3 Data Analysis

Before presenting the results, this section describes the systematic analysis used to extract the Absorbance peak resonance and its characteristics such as the full width at half maximum (FWHM) and the integrated intensity.

One starts by the fundamental quantitative spectroscopy law [22], named Beer-Lambert law which is found empirically and links the *transmittance* $T(\tilde{\nu})$ to a decreasing exponential depending on a *linear absorption coefficient* $\alpha(\tilde{\nu})$ and the thickness d of the sample at a given wavenumber $\tilde{\nu}$.

$T(\tilde{\nu})$ is defined by the ratio of the emerging radiant power just after passing through the sample $I(\tilde{\nu})$ to the incident radiant power before penetration $I_0(\tilde{\nu})$, the Beer's law is thus written as

$$T(\tilde{\nu}) = \frac{I(\tilde{\nu})}{I_0(\tilde{\nu})} = e^{-\alpha(\tilde{\nu})d}. \tag{3.1}$$

Note, usually the Beer's law is expressed in base 10. As presented in the **section 2.1**, the incident and emerging radiative power is obtained by performing the Fourier transform of the interferogram. For low energy, *i.e.*, in the far infrared region, the reference $I_0(\tilde{\nu})$ taken is a measure at high temperatures ($\approx 40\,\mathrm{K}$), when for mid infrared region the reference is the signal without the sample and cryostat, called *void* thereafter.

The napierian *absorbance* $A(\tilde{\nu})$ quantity is derived by taking the Napierian logarithm of the inverse transmittance in order to extract the characteristic $\alpha(\tilde{\nu})$, one has

$$A(\tilde{\nu}) = \log(1/T(\tilde{\nu})) = \alpha(\tilde{\nu})d. \tag{3.2}$$

The integrated peak absorbance $\mathcal{A}$, named *integrated intensity* thereafter reflects the strength of the resonance and is simply given by $\mathcal{A} = \int_{\mathrm{band}} A(\tilde{\nu})\mathrm{d}\tilde{\nu}$.

Lineshape and integrated intensity will be then used to describe a transition. In next subsections, noise reduction, profile fitting and transition assignment are presented.

3.1 Averaging and smoothing

Depending on the resolution and the energy range selected, a huge amount of data can be collected. Indeed, one measure can contain millions of data points. To reduce noise, around fifty measures were taken per configuration. Here are the steps followed :

(1) Average all the files corresponding to the same configuration.

(2) Depending on the transition we are interested in, the resolution could be decreased to obtain smaller signal to noise ratio. A simple median filter with a given binning is applied.

(3) Apply a smoothing function such as the Savitzky-Golay, a moving average filter.

Note the median is preferred than average because of the randomness of noise intensity. Note also this method does not significantly affect the fitting process, since it is basically only averaging. The smoothing step (3) is not applied when the fits are computed. An illustration of step (2) and (3) is shown on the Fig.3.1 where the transmission signal depending on the wavenumber and its associated absorbance are plotted. The process highlights clearly the resonance. One will discuss this results later in section **4.3**, since the energy range chosen presents a peculiarity which is a temperature-dependent peak position.

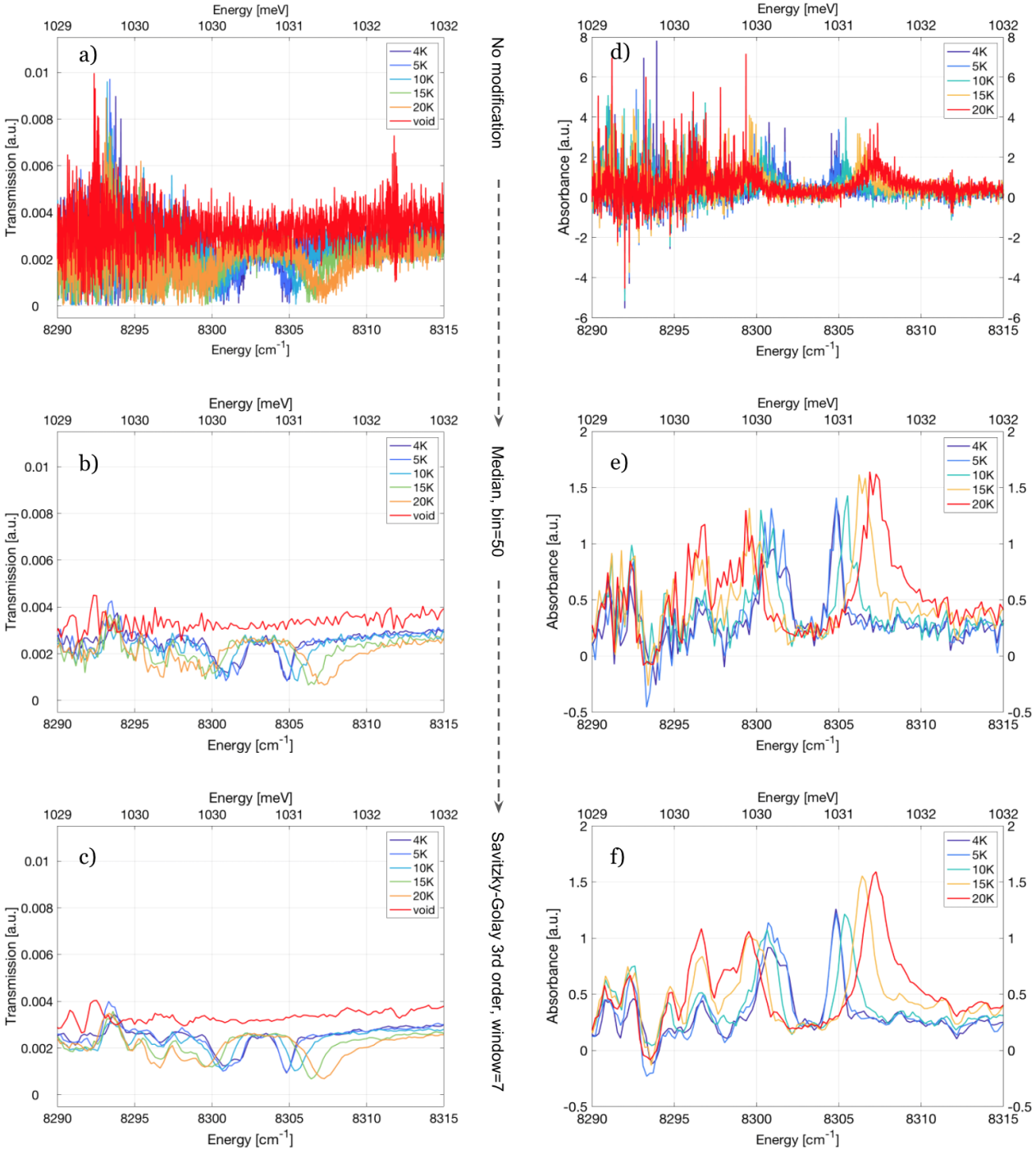

Figure 3.1 – Highlighting peak resonance process using noise reduction by taking the median and applying a Savitzky-Golay smoothing function. Detector=InSb, BS=3.5 μm Mylar, Polarization=//, resolution=0.01 cm^{-1}, aperture=1.3 mm.

3.2 Profile fitting

Two kinds of broadening process can appear : homogeneous and inhomogeneous. The homogeneous mechanism is related to effects which broad the linewidth of a transition by affecting radiation or emission in equivalent manners. On the opposite, inhomogeneous broadening relates to a process which increases linewidth depending on the acting atoms.

Inhomogeneous broadening

As introduced this type of broadening interacts differently depending on the absorbing atoms. Especially when the temperature is increased, thermal motion of the atoms arises and the ions start to interact with their nearest neighbour leading to an inhomogeneous broadening described by a Gaussian distribution.

$$\mathcal{G}(\tilde{\nu};\tilde{\nu}_0,\sigma) = \frac{1}{\sigma\sqrt{2\pi}} e^{-\frac{(\tilde{\nu}-\tilde{\nu}_0)^2}{2\sigma^2}} \tag{3.3}$$

where $\tilde{\nu}_0$ is the resonant peak position and σ the standard deviation.

Natural broadening

When an electron is in an excited state, after a certain time called *lifetime* it returns spontaneously to a lower energy state. Since the energy difference between the two states is quantized the photon energy absorbed or emitted is also quantized. Nevertheless due to the Heisenberg uncertainties the energy can be shortly violated. Hence not only one wavelength can be absorbed or emitted and thus it creates a specific profile, characterizing the absorbance depending on the energy instead of a δ function.

Assuming the probability to be in the initial state is proportional to a an exponential decay, expressed by

$$|\psi_i|^2 = e^{-\Gamma t}, \tag{3.4}$$

where ψ_i is the associated wave function, Γ the transition rate and $t > 0$ the time. It can be shown [23] that the spectral distribution intensity is a Lorentzian distribution given by,

$$\mathcal{L}(\tilde{\nu};\tilde{\nu}_0,\Gamma) = \frac{1}{2\pi}\frac{\Gamma}{(\tilde{\nu}-\tilde{\nu}_0)^2 + \frac{\Gamma^2}{4}} \tag{3.5}$$

Where for this profile the FWHM is Γ related to the *natural life time* τ by

$$\tau = \frac{1}{2\pi\Gamma}, \tag{3.6}$$

$\tilde{\nu}$ the variable wavenumber, and $\tilde{\nu}_0$ the energy center of the transition. The natural broadening is an homogeneous broadening since all transitions are concerned in equivalent manners.

Voigt Profile

Voigt profile $\mathcal{V}$ is defined as the convolution of a Lorentzian and a Gaussian distributions. The Voigt profile fitting is used in order to include the two broadening mechanisms. Mathematically, one has

$$\mathcal{V}(\tilde{\nu};\tilde{\nu}_0,\sigma,\gamma) = \mathcal{G} * \mathcal{L} = \int_{-\infty}^{\infty} \mathcal{G}(\tilde{\nu}';\tilde{\nu}_0,\sigma)\mathcal{L}(\tilde{\nu}-\tilde{\nu}';\tilde{\nu}_0,\gamma)\,\mathrm{d}\tilde{\nu}'. \tag{3.7}$$

Extracting the contribution of the Gaussian and Lorentzian distribution by fitting the absorbance peaks could therefore provide information about the broadening process. The full width at half maximum (FWHM) of the Voigt Profile α_V can be accurately approximated by [24]

$$\alpha_V = \frac{1}{2}\left[C_1\alpha_L + \sqrt{C_2\alpha_L^2 + 4\alpha_G^2}\right], \tag{3.8}$$

where $C_1 = 1.0692$ and $C_2 = 0.86639$, α_L and α_G are the widths of the Lorentzian and the Gaussian respectively. The Fig.3.2 shows the absorbance for the same energy level at two different temperatures. It can clearly be observed for low temperatures the lineshape follows a Lorentzian profile while for higher temperatures the Gaussian distribution fits better. This result is expected since thermal motion is drastically reduced at low temperatures. Voigt profile is thus a good fitting function candidate.

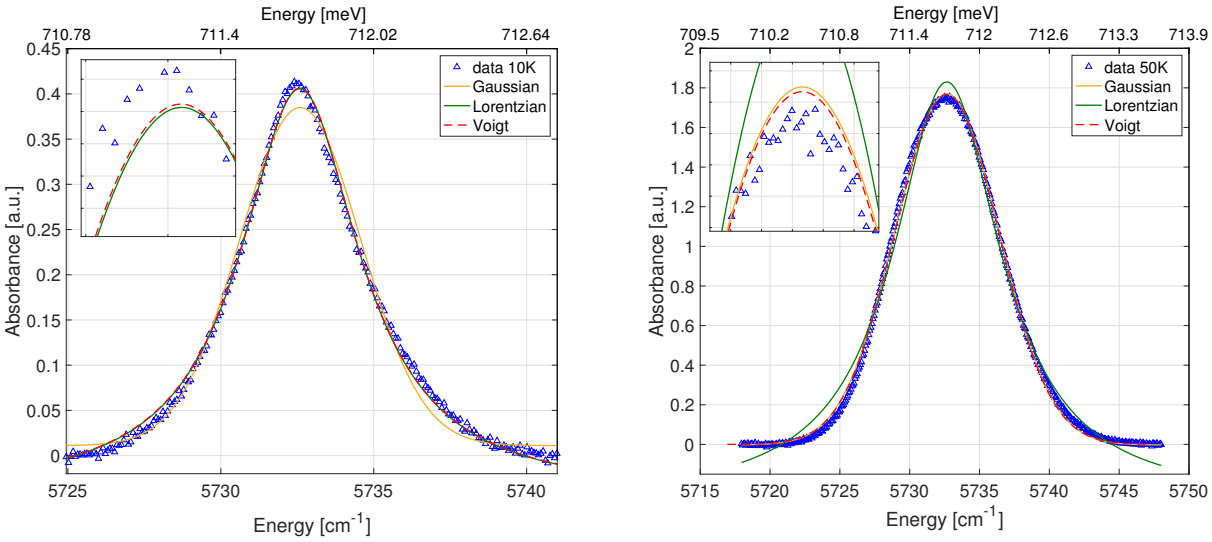

(a) T=10K (b) T=50K

Figure 3.2 – Detector=InSb, BS=CaF_2, polarization=//, resolution=0.03 cm^{-1}, aperture=1.7 mm

3.3 Transition assignment and selection rules

In general, a nominal temperature of 3.6 K is achieved by the helium cooling system in order to see only transitions from the ground state (Γ_2 symmetry). Indeed, by calculating the Boltzmann distribution, the ground state $^3H_{6.1}$ has more than 99.999 % of the total electron population. Even at this temperature, some transitions from the first excited state $^3H_{6.2}$ have been seen. Because of imperfections of the experimental setup, it is important to keep in mind that the nominal temperature can differ from the effective sample temperature.

A second set of measurements with increasing the temperature has been done such as to investigate other transitions coming from higher states $^3H_{6.2}$ and $^3H_{6.3}$. We can expect a more intense contribution for transitions which do not come from the ground state, since the electron population of higher energy levels increases with the temperature. While for GS transition, we may expect a decreasing contribution, represented by weaker absorption band.

Each manifold contains $2J + 1$ states. Due to the symmetry of the crystal (see Table 1.2) the number of observed transition lines is smaller, corresponding to degenetated states. Moreover, a transition may not be observed because of the selection rules. To assign the transition with its initial state, one used these following procedure :

(1) Identify all features which could be a transition in the absorbance spectrum at 3.6 K.

(2) As we know from Christensen (1979) measurements [12], numerical calculation and from our results (see **chapter 4**) the $^3H_{6.2}$ and $^3H_{6.3}$ state are approximately 31 cm^{-1} and 62 cm^{-1} respectively above the ground state, thus we start to look at transitions with an energy shift of theses ranges.

(3) By warming the sample, transitions from excited states become stronger and thus it highlights transitions from excited states.

(4) By comparing our results to the Christensen results.

(5) By comparing our results to the different numerical simulation.

Trying to unscramble the assignment puzzle in the best way, the results are presented in the next chapter.

To have a complete picture of the transition, the coupling between the electronic excitation and the incoming photon has to be determined. The excitation can occur through different interactions, electric-dipole, magnetic-dipole or higher orders. Selection rules dictates the most probable. For instance a electric dipole transition following $\Gamma_i \rightarrow \Gamma_i$ is forbidden with $i = 1, 2$. For magnetic dipole transition $\Delta J \leq 1$ and therefore transition from the $^3H_6$ manifold to $^3F_4$ cannot occur via a magnetic dipole transition. Unfortunately, this work does not present such assigment. More details can be found in Matmon's work [9] for a S_4 symmetry, present in $LiTmF_4$ crystal structure.

4 Results and discussion

This chapter presents the analysis of the electronic excitations in the far and mid-infrared of the first three manifolds $^3H_6$, $^3F_4$, $^3H_5$ in a pure $LiTmF_4$ crystal. In the following, the notation // and $\perp$ represent the z and x polarization respectively.

4.1 Far Infrared

This region corresponds to the lowest energy excitations. The bolometer detector cooled with liquid helium is used with a filter cutting higher energy, in combination with the 23 μm Mylar Beam Splitter. In this energy range, due to longer wavelengths and higher refractive index, Fabry-Perot interferences are clearly visible. The short oscillation in the Fig.4.1 and the big wiggles at the top of the Fig.4.2 and Fig.4.3 with a period of around 0.25 cm^{-1} and 10 cm^{-1} respectively come from the optics and the sample. Although, in certain cases, Fabry-Perot interferences can be comparable to the absorbance intensity, they do not significantly affect the fit since the interference are periodic and a least mean square fit is performed. However it gives rise to high fit uncertainties given by the 95% confidence interval, especially in the integrated intensity. In order to improve confidence of the fit, one can Fourier transform the transmission spectrum and remove the frequency caused by the Fabry-Perot interference. This process is shown in the Fig.4.1. As expected the fits are very similar even with the correction, but the uncertainties of integrated have been reduced.

Only the electronic excitations occurring inside the $^3H_6$ manifold are expected to be found in that measurement. Indeed, because of the spin orbit interaction the second manifold is separated by almost 6'000 cm^{-1} and stands in higher energy, in the mid infrared.

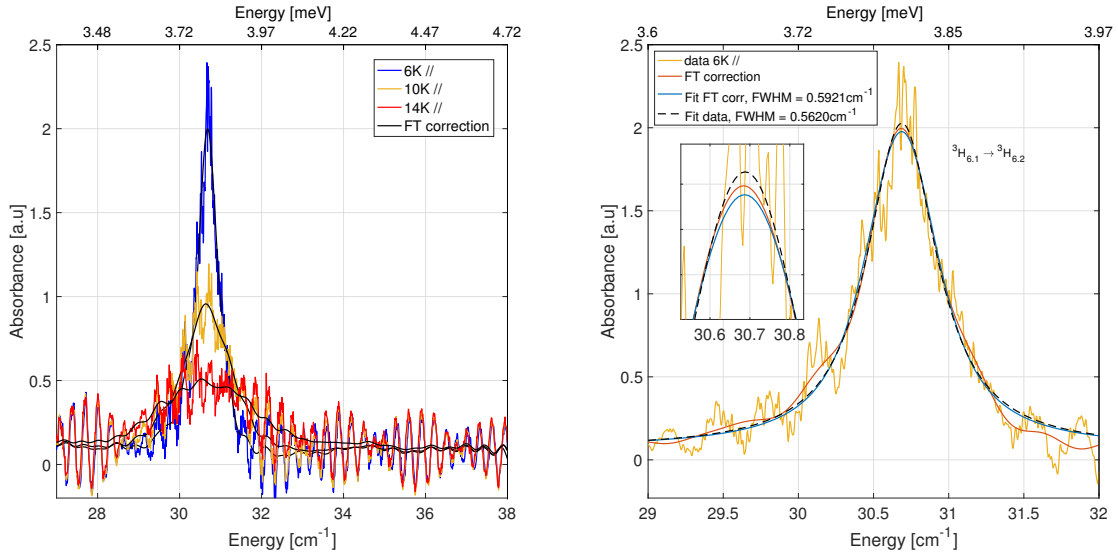

Figure 4.1 – Left: Data corrected by removing the frequency due to Fabry-Perot interferences. Right: fitting method comparison by taking raw data and corrected data for T=6 K.

4.1.1 $^3H_6$ manifold

The first manifold of the $LiTmF_4$ is given by Hund's rules ($J = 6$) and has $2J + 1 = 13$ states decomposed in $3\Gamma_1 + 4\Gamma_2 + 3\Gamma_{34}$ irreducible representations according to the Table 1.2.

Only the first three transitions have been observed because of the setup limitations. The Fig.4.2 and Fig.4.3 shows respectively the transmission and the absorbance measured for parallel and perpendicular polarization. For both polarizations the absorption of the first transition is very strong. Especially for the x polarization measurement where the crystal absorption for the first ($30.8\,cm^{-1}$) and second ($68.8\,cm^{-1}$) transition becomes too high and no clear analysis can be performed. Even when the temperature is increased and depopulate the ground state, the absorption remains too strong. At the opposite, the third transition around ($291.7\,cm^{-1}$) is very barely observable for the x polarization data and invisible for the parallel measurement. One would expect to strengthen that transition by increasing the temperature. Although the absolute transmission values are lower, the dip present at low temperature, in the right inset of the Fig.4.3, vanishes. One should note that the transmitted beam is close to zero, therefore we should not do early conclusion. A thinner sample would probably solve this issue.

The triplet around $202\,cm^{-1}/25.1$ meV in the z polarization configuration is probably caused by ambient environment since it is not temperature-dependent. However, it is intriguing to not be able to observe this triplet in perpendicular polarization data. The transmitted signal is again very weak and may be the cause.

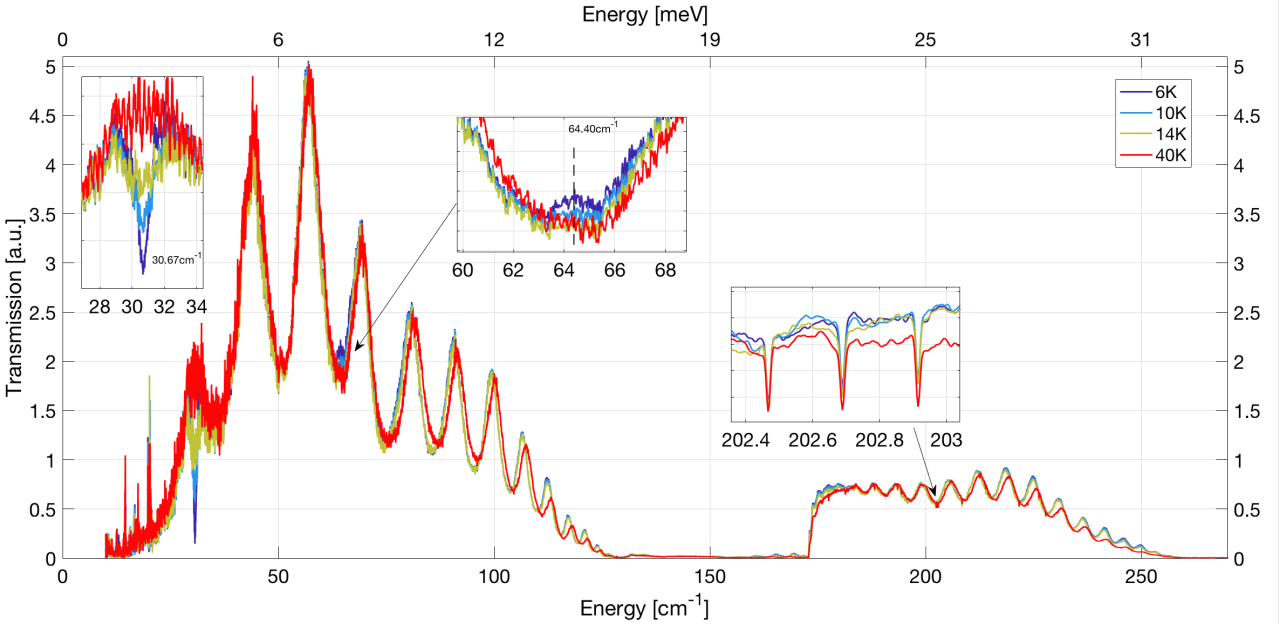

(a) Transmission

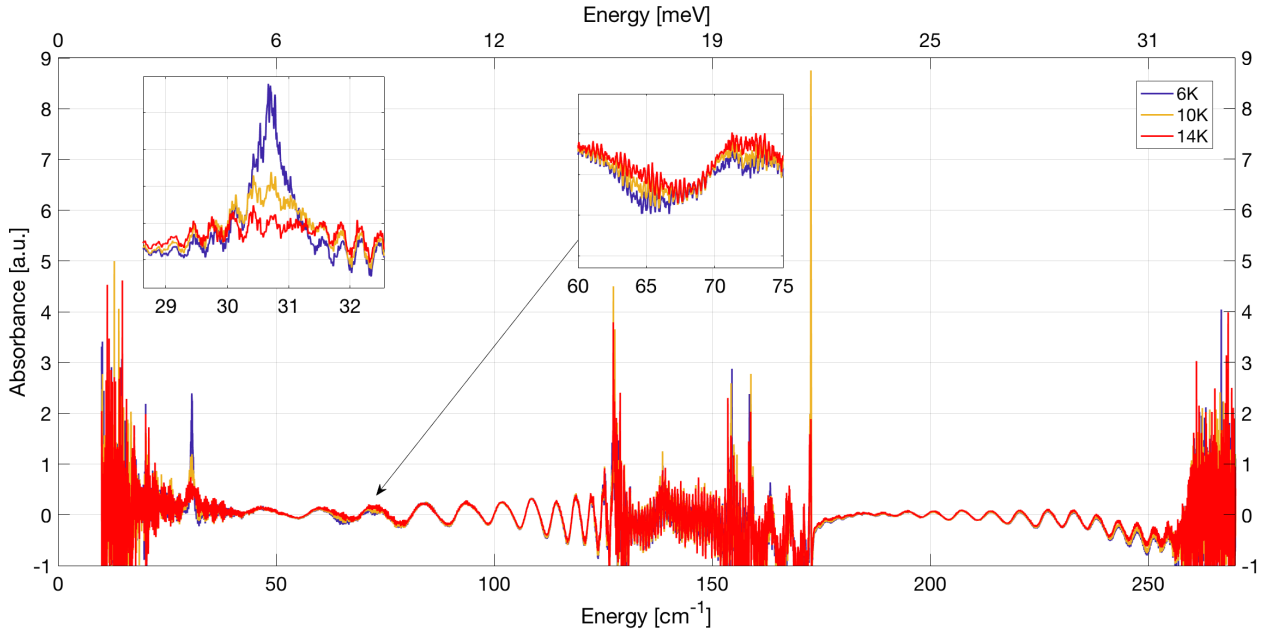

(b) Absorbance

Figure 4.2 – Detector=Bolometer, BS=23 μm Mylar, polarization=//, resolution=0.01 cm^{-1}, aperture=5 mm

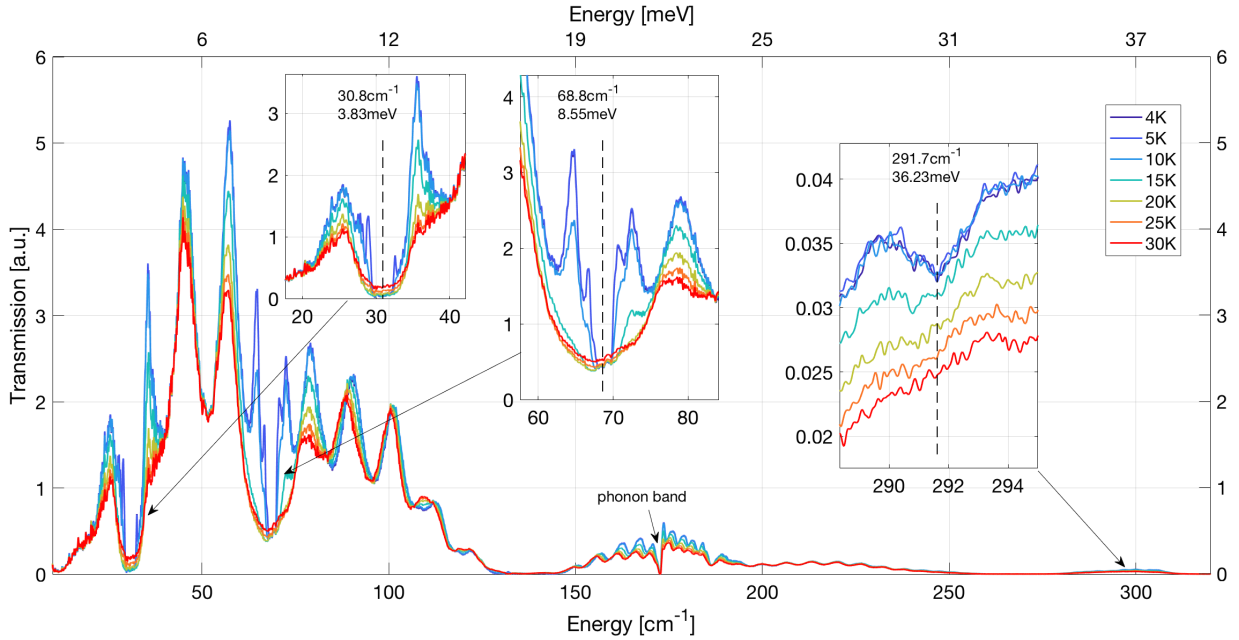

(a) Transmission

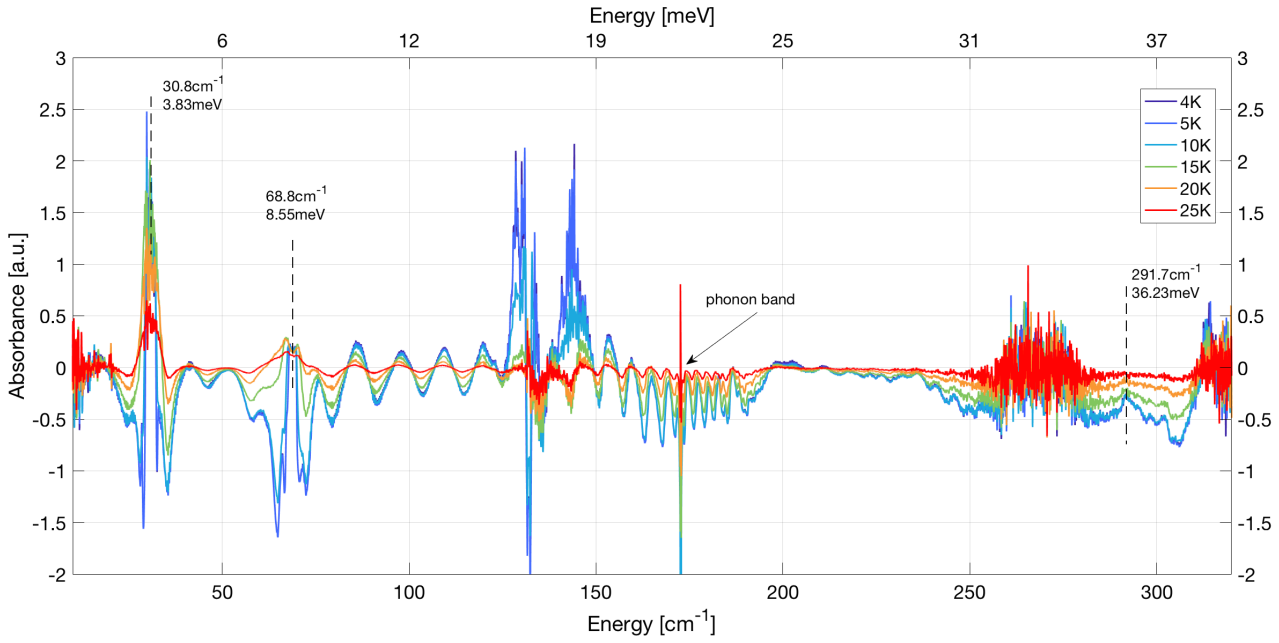

(b) Absorbance

Figure 4.3 – Detector=Bolometer, BS=23 μm Mylar, polarization=$\perp$, resolution=0.01 cm^{-1}, aperture=5 mm

The only suitable peak for a precise analysis is the first transition at $30.67\,\mathrm{cm}^{-1}$ in z polarization configuration. The evolution of the first transition depending on the temperature is presented in Fig.4.4. The peak position (left graph) shows a complete independence as expected in that low energy regime. Indeed, no drastic modification of the effective Hamiltonian has been triggered and hence we would expect to have the same energy difference between the states. An example of a peak temperature-dependent is discussed in **subsection 4.2.2**. The integrated intensity in function of the temperature is plotted on the right graph. A clear correlation appears. It can be explained by the depopulation of the ground state, since the electronic population follows the distribution of Fermi-Dirac, leading to a reduction of the probability of transition. It would have been interesting to fit the data and find the correspondence between the population of the ground state and the intensity of that transition.

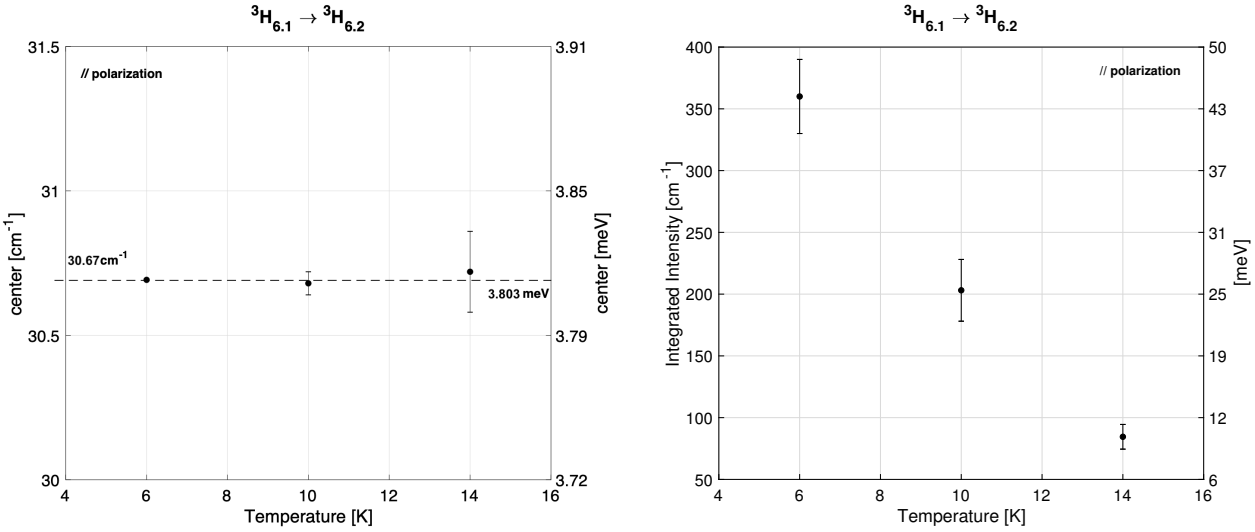

Figure 4.4 – Left: peak position temperature independent. Right: reduction of the strength because of the electronic depopulation of the ground state.

In the energy range between $150\,\mathrm{cm}^{-1}$ and $200\,\mathrm{cm}^{-1}$ a curious feature occurs for perpendicular polarization, the intensity of the transmitted light seems to depend strongly on the temperature. It can not be attributed to the refractive index of the sample which is temperature-depend, since for parallel polarization this feature does not appear in similar way. The question remains open. Moreover, by comparing the two polarization measurements differentiated only by the way of orienting the crystal,the transmission appears to be weaker, in average, for the perpendicular case. The observation makes even more intriguing that temperature dependent effects. A zoom of region of interested is shown in Fig.4.5. In the same region, in both measurement, a really sharp absorption is observed around $173\,\mathrm{cm}^{-1}$. This energy range corresponds to phonon excitations, in Babkevitch study a similar feature is present at the same energy and has been assigned to a phonon band.

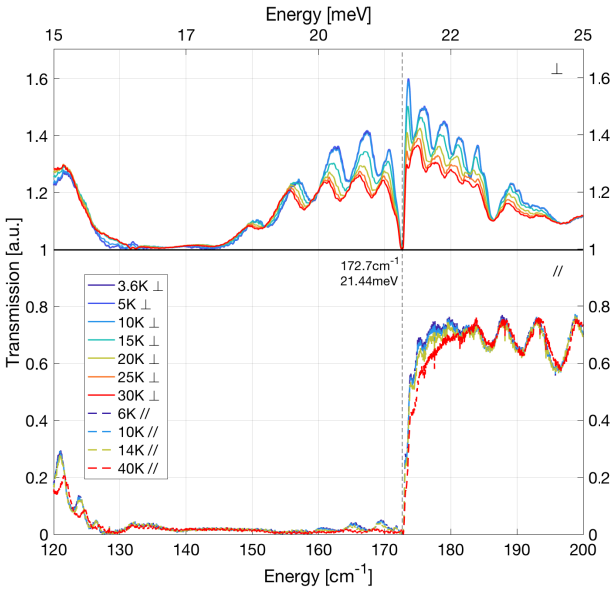

Figure 4.5 – Zoom on the energy region between $150\,\mathrm{cm}^{-1}$ and 200 where a strong absorption occurs in both polarization and is attributed to a phonon band.

The Table 4.1 summarized the observed transitions inside the first manifold. The second column correspond to neutron scattering experimental results from Babkevitch *et al.* (2015). All transitions observed agree with the previous results and the relative difference is smaller than 4 %. At the exception of the ${}^3H_{6.3}$ line where for the x polarization measurements the difference is around 12 %. The deviation of the later is not understood. However, those results are to take with precaution, since the absorption by the crystal in this energy range is very strong, which saturates the signal. Moreover, other artefacts like Fabry-Perot interferences could hide the true signature.

State			Obs. transitions			
Index	Energy [7] [cm^{-1}]	Symmetry	Initial State	Polarization	Energy [cm^{-1}]	Int. intensity [cm^{-1}]
${}^3H_{6.1}$	0	Γ_2				
${}^3H_{6.2}$	31.72	Γ_{34}	${}^3H_{6.1}$	x	(30.8 ± 0.5)	-
				z	$(30.67 \pm 0.02)^*$	$(360 \pm 30)^*$
${}^3H_{6.3}$	61.66	Γ_1	${}^3H_{6.1}$	x	(68.8 ± 1.5)	-
				z	(64.4 ± 1.5)	-
${}^3H_{6.4}$	293.0	Γ_2	${}^3H_{6.1}$	x	(291.7 ± 0.5)	-
				z	-	-

Table 4.1 – Observed transitions in the ${}^3H_6$ ground manifold. *Only this level has been correctly fitted, the rest is given by *visual* consideration.

4.2 Mid and Near Infrared

The second $^3F_4$ and third $^3H_5$ manifolds are located around $5'700\,cm^{-1}$ and $8'300\,cm^{-1}$ respectively above the ground state, which corresponds to the mid and near infrared regions. It turns out the indium antimonide detector was the most sensitive to investigate the two manifolds. Therefore, the same configuration has been set up and two beam splitters (BS) were tested, the CaF_2 and the mylar beam splitter with a thickness of 3.5 mm.

The Fig.4.6 and Fig.4.7 show the raw transmission and its associated absorbance spectrum for parallel polarization (z) using the CaF_2 and the mylar beam splitter. It highlights the effect of the beam splitter. The absorption around $4'000\,cm^{-1}$ is caused by optic elements within the interferometer, since without the cryostat (*void* data) the lineshape remains identical and presents no temperature dependence. Moreover, the feature is visible in both configuration. The cut-off energy around $3'500\,cm^{-1}$ is due to the limitation of the detector. In both configurations the second and the third are present, however the data from the CaF_2 beam splitter is preferred for the analysis since it provide better signal to noise ratio.

The peak assignments were done following the procedure described in **section 3.3** and are summarized in the Table 4.2 and Table 4.3 for the $^3F_4$ and $^3H_5$ manifolds respectively.

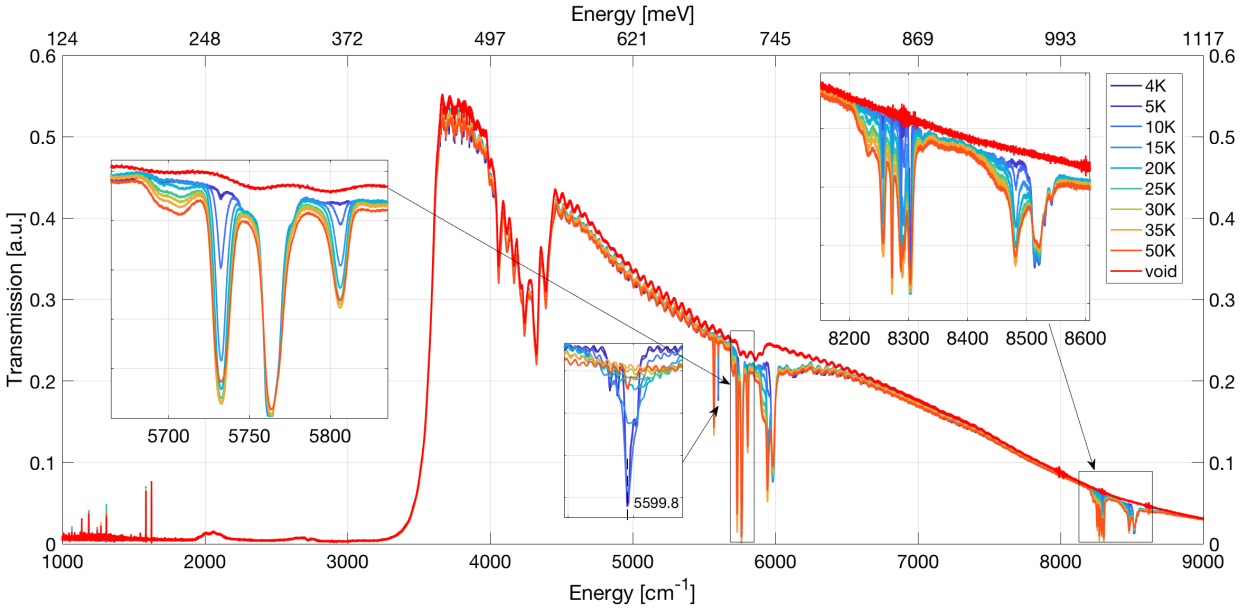

Figure 4.6 – Transmission data spectrum using the CaF_2 BeamSplitter, detector=InSb, polarization=//, resolution=$0.03\,cm^{-1}$, aperture=1.7 mm

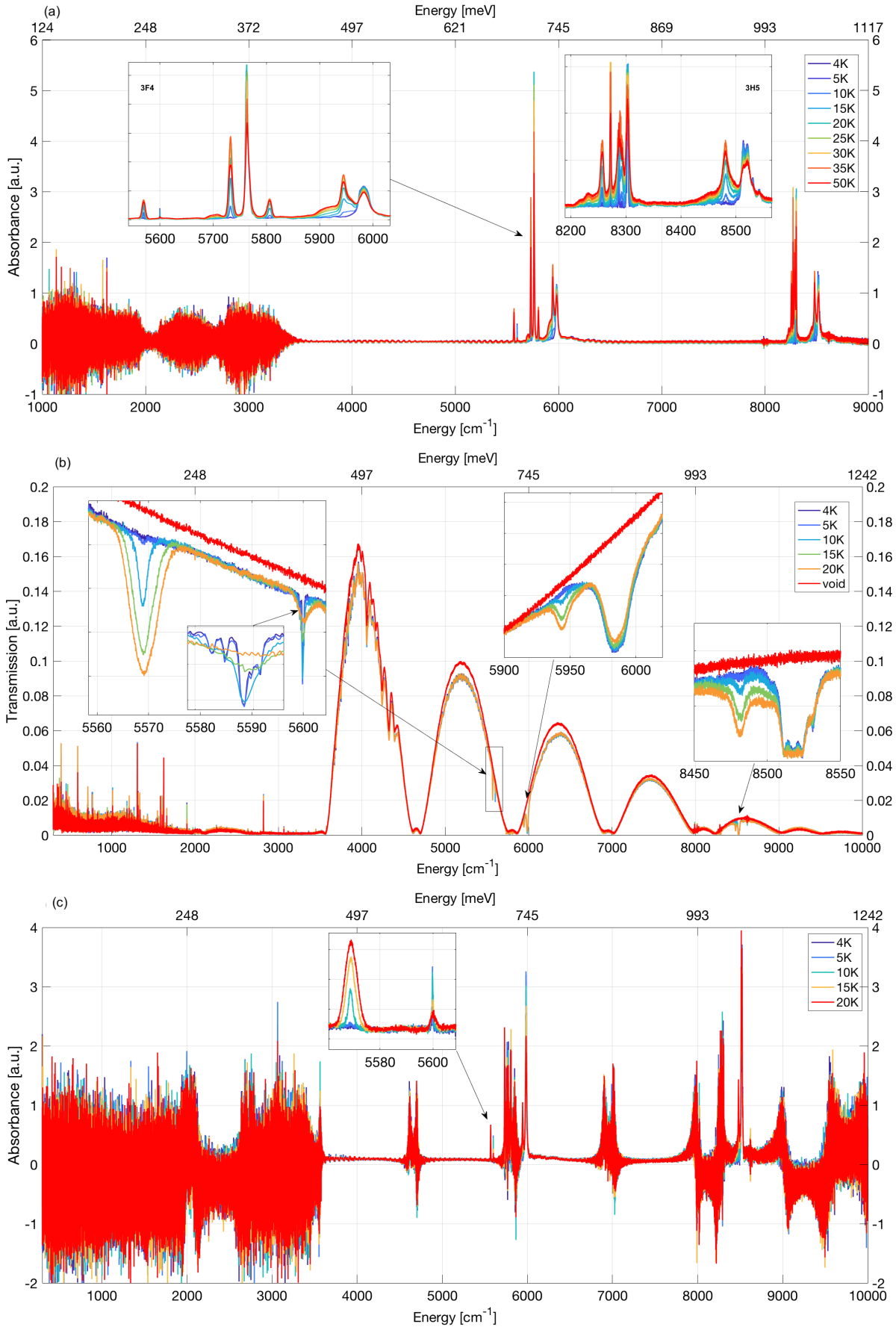

Figure 4.7 – Detector=InSb, polarization=//, resolution=0.03 cm^{-1}, aperture=1.7 mm, (a) absorbance spectrum using the CaF_2 BS, (b) Transmission data and (c) its associated absorbance spectrum using the 3.5mm Mylar BeamSplitter.

4.2.1 $^3\mathrm{F}_4$ manifold

The Fig.4.8 shows the second manifold where new transitions appear when the temperature is increased. Those transitions originate from the excited state $^3H_{6.2}$ and $^3H_{6.3}$. Indeed, their positions correspond to the expected value. To take one example, the energy difference between the main peak around $5763\,\mathrm{cm}^{-1}$ present at low temperature and the new peak around $5732\,\mathrm{cm}^{-1}$ appearing at higher temperature is around $31\,\mathrm{cm}^{-1}$. This energy shift corresponds to the energy difference between the ground state and the first excited level. One can conclude that this new transition occurs between the same arrival state but its initial state associated is the first excited state $^3H_{6.2}$. With the same logic, one expects to find new absorption lines at lower energy corresponding when increasing the temperature coming from the (more) excited state $^3H_{6.3}$ and so on. Indeed, at 25 K three new transitions are observed around $5920\,\mathrm{cm}^{-1}$ and are denoted in red $^3H_{6.3} \rightarrow^3 F_{4.5-7}$. Because of inhomogeneous broadening, the transitions tend to flatten and it is getting harder to distinguish them. Nonetheless, knowing the energy difference between the states in the first manifold, it is possible to perform a very good fit with a convolution of 9 peaks as depicted in the top of the Fig.4.9. This assumption is probably not be valid for very high temperature, since the effective Hamiltonian is expected to be modified by external perturbation such as crystal vibrations. At the bottom of the figure, the emergence of new peaks as the disappearance of others are well observed depending on the temperature in the 3D plot.

It is important to notice the birth of a resonance at $5805.8\,\mathrm{cm}^{-1}$, since no peak is found close to $5836.8\,\mathrm{cm}^{-1}(= 5805.8 + 31\,\mathrm{cm}^{-1})$. Although very unlikely, assuming a transition from the second excited state, no peak is found close to $5870\,\mathrm{cm}^{-1}$ either. With a deeper investigation, one remarks that its intensity increases with temperature which suggests a transition from an excited state and not the ground state. Moreover, according to symmetry and the total angular momentum (J=4) of that manifold, one expect to see 5 non-degenerate states and 2 doublets. However, only 6 transitions are clearly visible. In addition, the numerical calculation suggests the presence of one resonance from the GS close to $5836.8\,\mathrm{cm}^{-1}$, comforting the idea to have the transition $^3H_{6.1} \rightarrow^3 F_{4.4}$ that one can not see. It can be explained by the selection rule, $^3F_{4.4}$ has a Γ_2 symmetry like the ground state. Therefore electric and magnetic dipole transition are forbidden, but $^3H_{6.2}$ has a Γ_{34} symmetry. Hence this coupling is allowed for an electric dipole transition. Finally, we attribute the resonance $5805.8\,\mathrm{cm}^{-1}$ to the transition $^3H_{6.2} \rightarrow^3 F_{4.4}$ and deduce the position of the $^3F_{4.4}$ state indicated by the yellow dashed line on the Fig4.8.

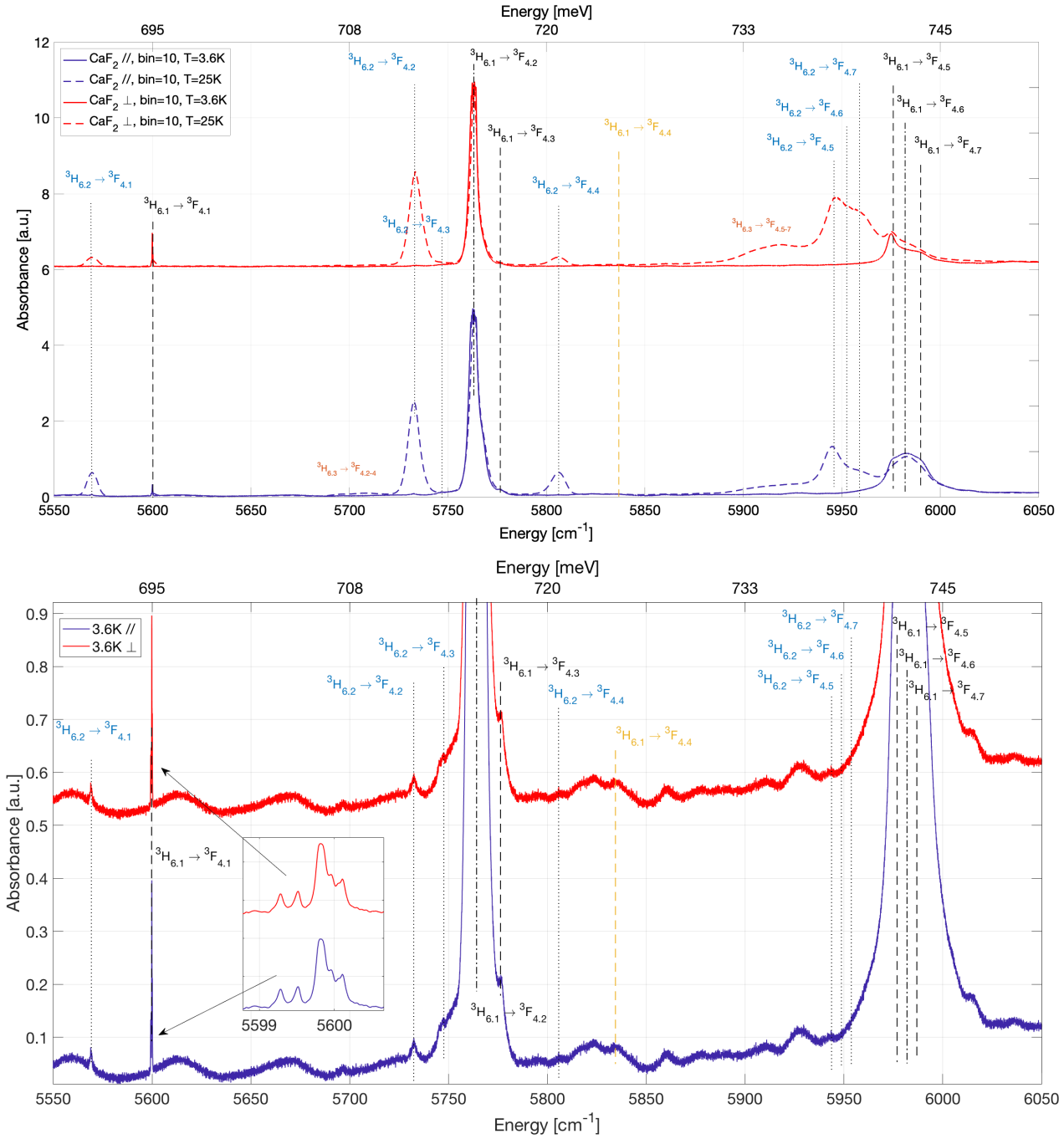

Figure 4.8 – Transitions from the ground manifold to the $^3F_4$ manifold, Detector=InSb, BS=CaF_2, resolution=0.03 cm^{-1}, aperture=1.7 mm.

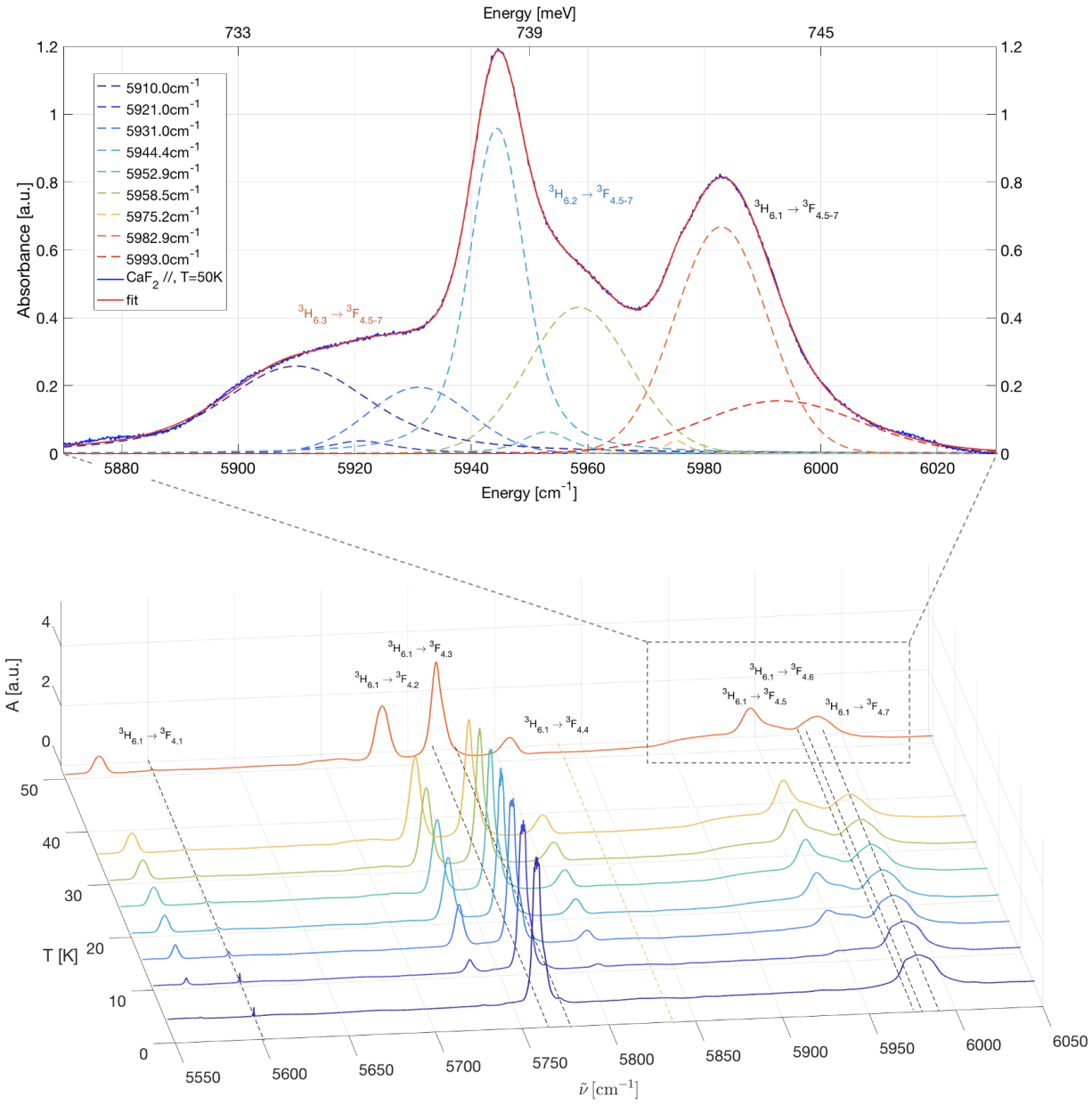

Figure 4.9 – top: convolution of nine Voigt profiles corresponding to all possible transitions between ${}^3H_{6.1-3}$ and ${}^3F_{4.5-7}$ states. bottom: absorbance spectrum for different temperatures, Detector=InSb, polarization=//, resolution=0.03 cm^{-1}, aperture=1.7 mm, BS=CaF_2.

One has chosen to investigate the evolution of the transition ${}^3H_{6.2} \rightarrow {}^3F_{4.2}$ ($5732.5\,\mathrm{cm}^{-1}$). The center of the selected transition does not show any dependence on the temperature. More generally, not center temperature dependent up to 50 K has been observed inside that manifold. The top Fig.4.10 demonstrates the process of broadening when increasing the temperature. It is possible to estimate precisely the contribution of the Gaussian and the Lorentzian distributions. Those contributions are represented in the middle panel. While the Gaussian contribution increases, the Lorentzian contribution remains constant. As discussed in the previous chapter, the Lorentzian profile is directly related to the life-time of the state. In the present case, the natural life time is temperature independent and the broadening comes from only inhomogeneous contributions. Using the Heisenberg uncertainties principles, we found a life time of few picoseconds for that transition.

A first attempt to resume the observed transitions is presented in the Table 4.2. Unfortunately, the table does not include yet all the transitions and needs to be completed.

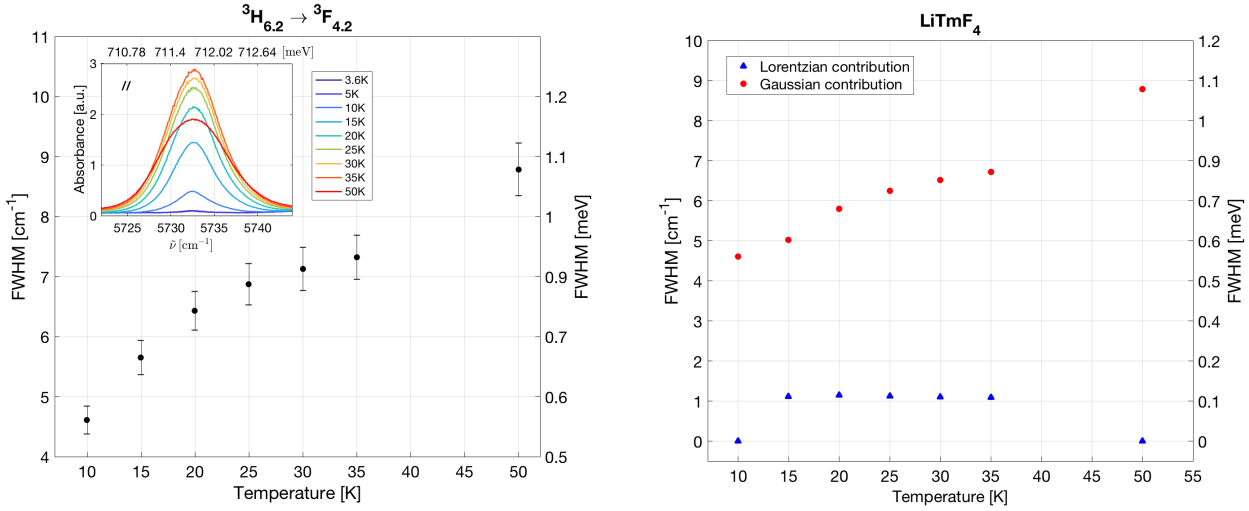

Figure 4.10 – top: total FWHM of the Voigt profile, bottom: distinct contributions between Gaussian and Lorentzian distribution.

The Fig.4.11 compares the obtained results of this manifolds to the numerical calculation of the best matched CF parameters from Romanova where the relative error is in average 0.11% and the absolute error is between $1.3\,\mathrm{cm}^{-1}$ and $12.2\,\mathrm{cm}^{-1}$, which is in good agreement for this manifold. It is important to mention that the numerical calculation is consistent with the experimental results. That confirms that our model taking in account the crystal field and the spin orbit interactions are in good agreement. Moreover, theoretical prediction was useful to complete the picture and deduce the missing transition because of selection rules. Nevertheless, the first doublet state expected numerically is actually two singlets experimentally as shown on the right figure where two Voigt profiles are needed to fit correctly the data. The splitting is around $5\,\mathrm{cm}^{-1}/0.62\,\mathrm{meV}$ and is too large to correspond to the hyperfine splitting. Its origin is probably because of imperfections within the crystal structure leading to lower the symmetry and resulting to the loss of degeneracy.

State			Observed transitions			
Index	Energy [12] [cm^{-1}]	Symmetry	Initial State	Energy [cm^{-1}]	Pol.	Int. intensity [cm^{-1}]
$^3F_{4.1}$	5585	Γ_1	$^3H_{6.1}$	$(5599.85 \pm 0.01)^*$	x	(0.53 ± 0.02)
				$(5599.86 \pm 0.01)^*$	z	(0.23 ± 0.01)
$^3F_{4.2a}$	5757	Γ_{34}	$^3H_{6.1}$	(5762.85 ± 0.04)	x	(26.86 ± 3.64)
				(5762.87 ± 0.05)	z	(28.68 ± 3.45)
$^3F_{4.2b}$	-			(5768.42 ± 0.41)	x	(1.93 ± 0.09)
				(5768.09 ± 0.22)	z	(6.73 ± 0.26)
$^3F_{4.3}$	5757	Γ_1	$^3H_{6.1}$	(5776.68 ± 1.82)	x	(0.07 ± 0.01)
				(5776.69 ± 1.25)	z	(0.22 ± 0.01)
$^3F_{4.4}$	5828	Γ_2	$^3H_{6.1}$	$(5836.70 \pm 0.55)^{**}$	x	-
				$(5836.60 \pm 0.03)^{**}$	z	-
			$^3H_{6.2}$	(5805.76 ± 0.05)	x	(2.00 ± 0.24)
				(5805.89 ± 0.03)	z	(5.14 ± 0.44)
$^3F_{4.5}$	5957	Γ_1	$^3H_{6.1}$	(5974.69 ± 0.06)	x	(1.48 ± 0.03)
				(5975.18 ± 0.11)	z	(0.80 ± 0.01)
			$^3H_{6.2}$	(5946.80 ± 0.29)	x	(5.95 ± 0.32)
				(5944.74 ± 0.07)	z	(2.33 ± 1.23)
			$^3H_{6.3}$	-	x	-
				(5903.05 ± 7.89)	z	(3.21 ± 11.21)
$^3F_{4.6}$	5961	Γ_2	$^3H_{6.1}$	(5975.80 ± 0.48)	x	(4.32 ± 0.52)
				(5980.78 ± 0.56)	z	(16.14 ± 2.08)
			$^3H_{6.2}$	(5955.62 ± 1.78)	x	(16.23 ± 2.12)
				(5953.74 ± 1.52)	z	(10.53 ± 1.79)
			$^3H_{6.3}$	-	x	-
				(5911.57 ± 7.89)	z	(0.75 ± 8.42)
$^3F_{4.7}$	5965	Γ_{34}	$^3H_{6.1}$	(5985.67 ± 0.41)	x	(5.87 ± 0.82)
				(5990.43 ± 0.31)	z	(9.77 ± 1.63)
			$^3H_{6.2}$	(5960.41 ± 0.26)	x	(0.24 ± 0.41)
				(5960.81 ± 0.79)	z	(0.10 ± 0.20)
			$^3H_{6.3}$	-	x	-
				(5923.51 ± 16.09)	z	(4.01 ± 13.34)

Table 4.2 – For the initial state $^3H_{6.1}$, $^3H_{6.2}$, $^3H_{6.3}$ the measure at T=3.6 K, T=15 K, T=25 K have been respectively used. No tangible values have been found in x polarization for the transition $^3H_{6.3} \rightarrow^3 F_{4.5}$.
*The data at T=10 K are used for the fit.
**These transitions was deduced from the transition $^3H_{6.2} \rightarrow^3 F_{4.4}$ and the energy corresponding to $^3H_{6.1} \rightarrow^3 H_{6.2}$ has been subtracted. An approximately constant deviation of around $+15\,cm^{-1}$ is found between the Christensen values our results.

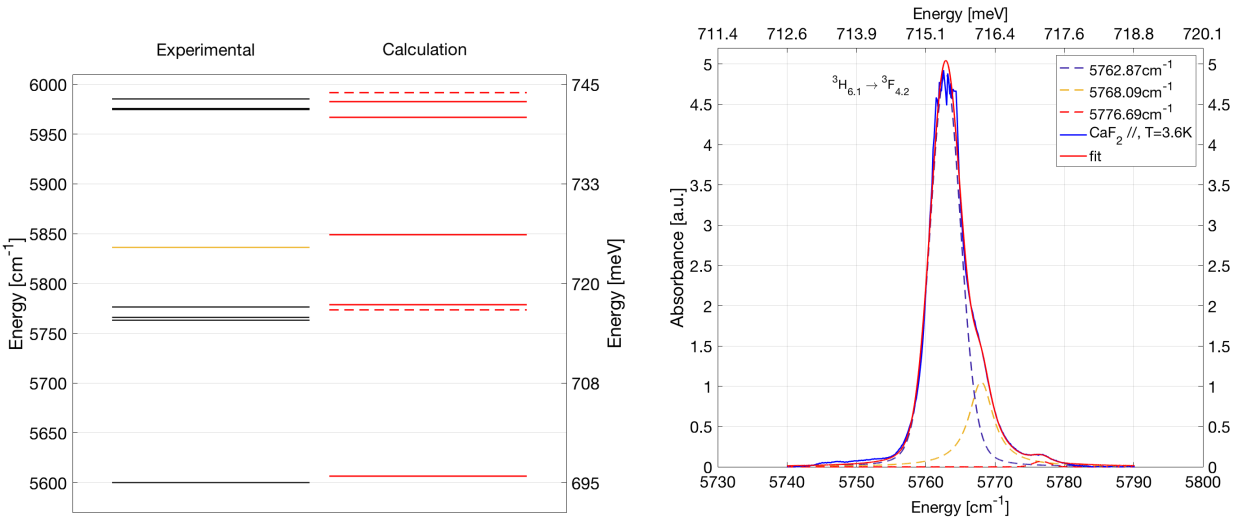

Figure 4.11 – left: In red the calculated energy levels from Romanova [10] CF parameters. Dashed lines represented doublet state. In black the experimental data found in that work. In yellow the expected level deduced by its excited level. Right: Splitting of the numerically expected doublet state, BeamSplitter= CaF_2, detector=InSb, polarization=//, resolution=0.03 cm^{-1}, aperture=1.7 mm.

Another splitting is found at 5600 cm^{-1}. The splitting is visible for the two polarizations. The Fig.4.12 shows a set of 6 peaks at low temperature of the first state of the manifold (Γ_1). However the energy difference between each center is much smaller, of the order of tens of μeV. Above 10 K, the splitting is no more distinguishable due to the Doppler broadening effect. The origin may comes from the hyperfine interaction. Indeed, referring to the Table 1.1, thulium has a nuclear spin I = 1/2 which can lead to a hyperfine splitting of 2I + 1 = 2 states. However, six peaks are observed. Although Thulium posses 35 known isotopes it is a monoisotopic element. The others isotopes have different nuclear spin which could create new hyperfine splitting and match the number of peaks observed. Nevertheless, to achieve that configuration, it would mean that the Thulium sample decays. In that perspective, the irradiation of the sample could trigger the decay. However it is very unlikely because of the energy insufficiency to activate a nuclear reaction. Moreover, in comparison to a another set of measurements in the sample of $LiY_{1-x}Ho_xF_4$ with $x = 0.01\,\%$, the isotopic splitting caused by the lithium ion observed has a difference energy of around one μeV which is one order of magnitude lower. The question of this splitting origin remains open.

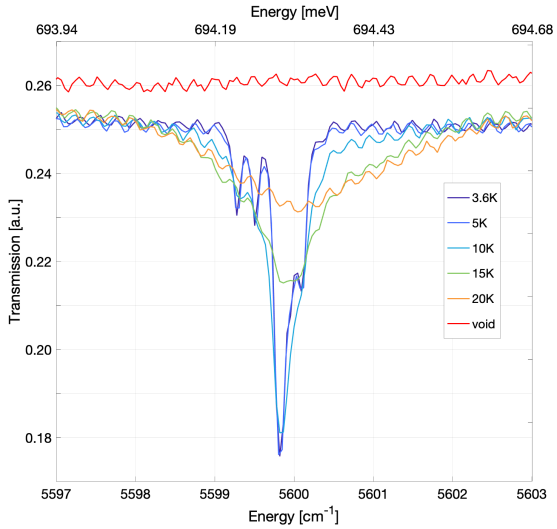

(a)

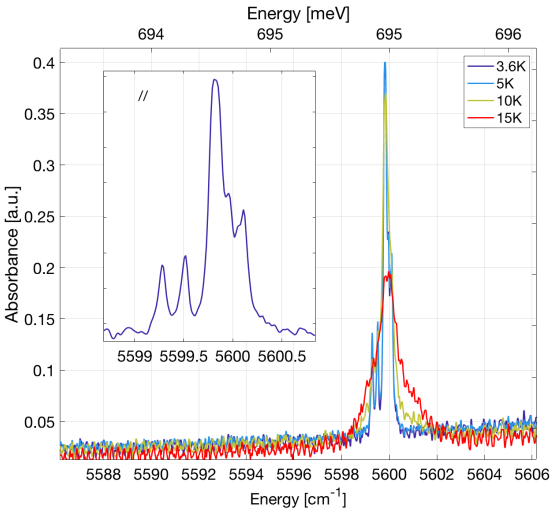

(b)

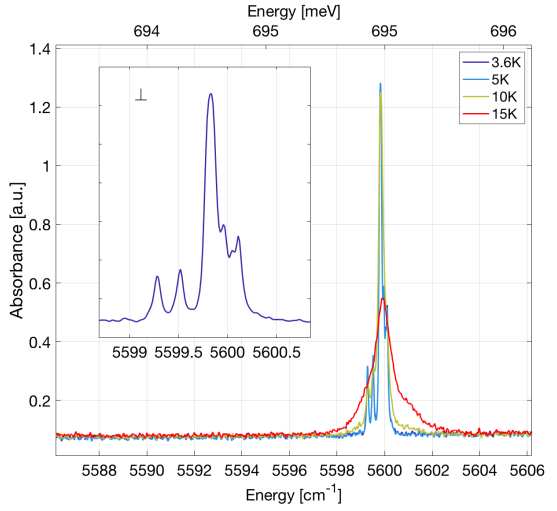

(c)

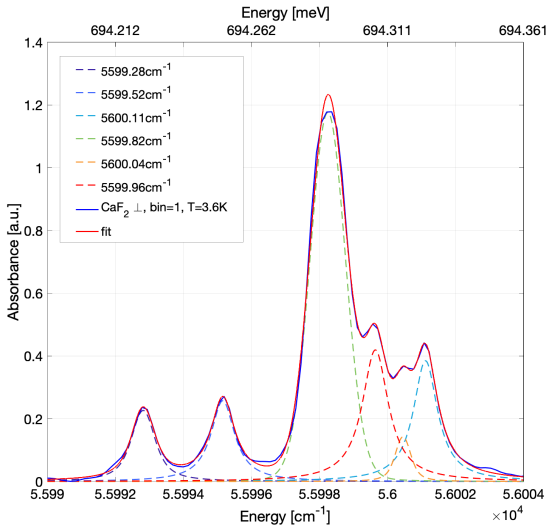

(d)

Figure 4.12 – Detector=InSb, resolution=0.03 cm^{-1}, aperture=1.7 mm, BS=CaF_2. Splitting of the $^3F_{4.1}$ energy level (a) transmission data, polarization=// (b) with its associated absorbance. (c) absorbance data with x polarization. (d) Fit of the 6 observed peaks using 6 Voigt profiles.

4.2.2 $^3\mathrm{H}_5$ manifold

This manifold corresponds to the highest energy manifold investigated in this work. The same analysis procedure as the $^3F_4$ manifold is followed. The main results are displayed in Fig.4.13 and Fig.4.14. However, $^3H_5$ manifold is more complex and its interpretation more difficult, because of missing peaks and signal saturation.

To start, a potential splitting appear in the first energy level (Γ_2) shown in Fig.4.13(b) and (c). The expected first excited state is a singlet according to our numerical calculation. It is not clear if this splitting is an artefact or is real since the transmission signal is saturated and small. One should pay attention to the other satellite absorptions around the main peak. The only possible observation is that the presence of the peaks can only emerge from the sample and not from the instrument.

Looking now to the second energy level, a doublet state is expected. This energy level has been presented in the precedent chapter and its transmission and absorbance data are plotted in Fig.3.1. The filtering process highlights two centers which show a temperature-dependent position while a doubly degenerate state with only one center is expected according to the numerical results. At 4 K, the energy difference is around $3\,\mathrm{cm}^{-1}$ and is similar to the energy difference seen in the $^3F_4$ manifold where the loss of degeneracy of the state was caused because of the crystal imperfection. The same assumption can be made here and therefore the loss of degeneracy is attributed to a lower symmetry than the one considered in the numerical model. It is interesting to note that the gap between the two center become larger when increasing the temperature which means that each center has an opposite temperature dependence. Their "center of mass" remains constant. We can try to explain this phenomenon including phonons contribution. Indeed, by increasing the temperature, one expects to introduce distort due to the lattice vibration and therefore change the crystal orientation. This hypothesis reinforces the assumption of the origin of the splitting. Although the lineshape of the splitting of the doublet state in $^3F_4$ manifold does not show a distinct temperature dependent behaviour, the same consideration can be done. Further work needs to be done to de-convolute the two peaks and determine the presence or not of a temperature dependence.

Unlike the previous manifold, one remarks a strong intensity dependence on the light polarization, which indicates different coupling mechanisms. A total of 8 distinct transitions have been assigned and at least one is missing. Looking at the numerical expectations, the transition should located in the upper i.e. highest energy part of the manifold. As a result of convoluted transition, it is difficult to clearly identify a new peak that might me hidden in the lineshape. In our first attempt, we have considered the possibility that the missing transition is either hidden because of the presence of the other peaks or either can not be detected because of experimental limitation. In that option, the the transition $^3H_{6.1} \rightarrow^3 H_{5.7}$ does not have the same energy between the two polarization. However, the key could be that, actually there are two different transitions which are respectively not visible for one polarization to the other because of selection rules. Unfortunately, all transitions from the second excited state $^3H_{6.2}$ the temperature have been assigned and therefore the identification of the missing peak remain unsuccessful. The temperature dependence of the $^3H_5$ manifold is presented in the Fig.4.14.

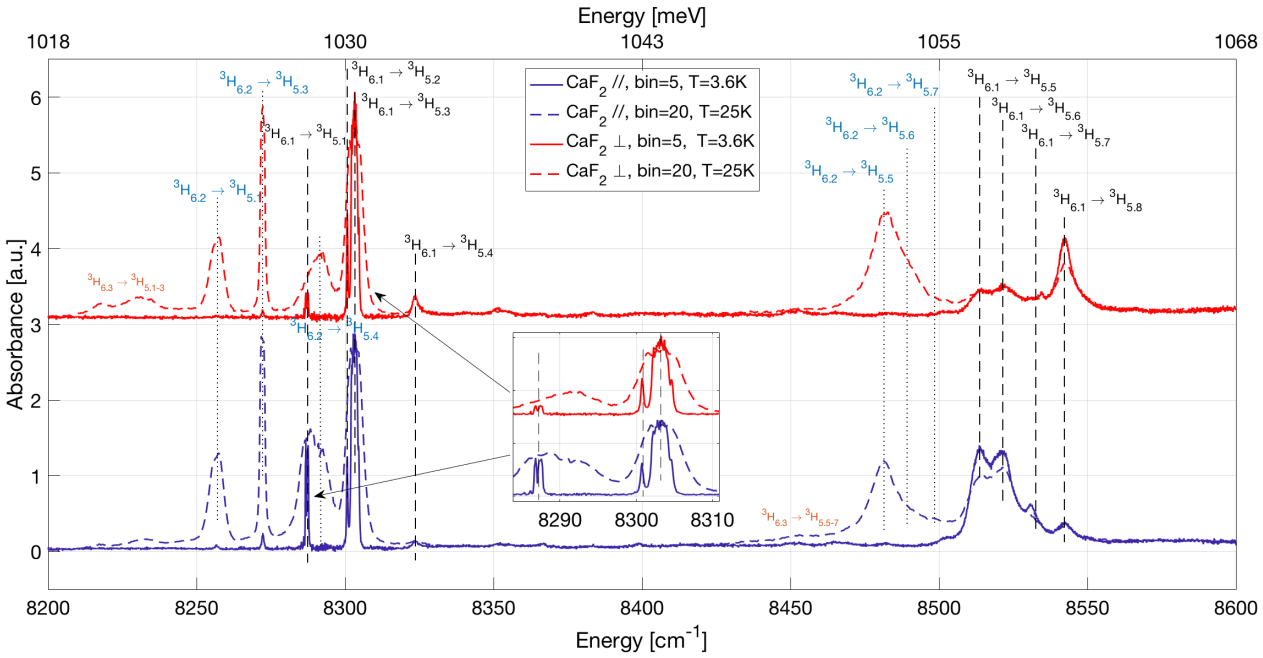

(a)

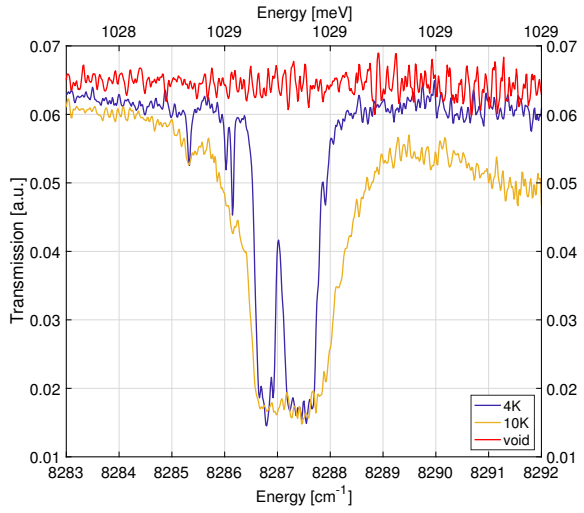

(b)

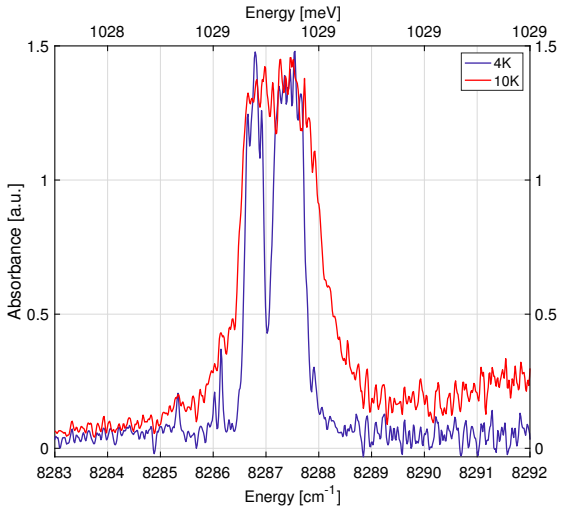

(c)

Figure 4.13 – detector=InSb, BS=CaF_2, resolution=0.03 cm^{-1}. (a) Absorbance spectrum of $^3H_5$ manifold (b) transmission and (c) absorbance of the first state with z polarization.

The Fig.4.15 right compare the obtained results to the numerical simulation. Although, the peak locations are in good agreement with the calculation (the relative error average is 0.5% and absolute error is comprised between 7.8 cm^{-1} and 180 cm^{-1}), at least one state is missing in the upper part $^3H_5$. A important thing to notice is a constant deviation of around +15 cm^{-1} in the same direction for both $^3F_4$ and $^3H_5$ manifolds in our results compare to the Christensen's results. Moreover, new peaks that Christensen did not succeed to measure have been observed analysed. The left graph shows the ability to produce a good fit even with saturated signal. A first try of transition assignments is given in Table 4.3. Further work is needed in order to completely unscramble the puzzle. Some ideas are given in the next and last chapter.

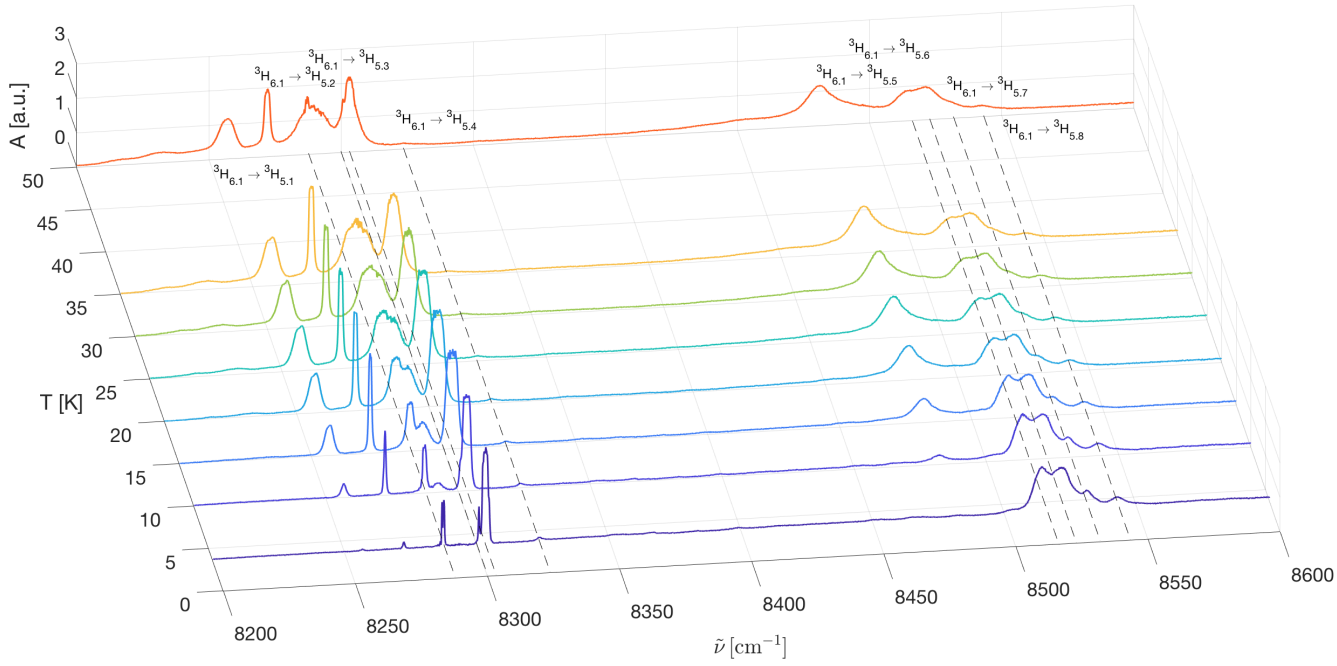

Figure 4.14 – absorbance spectrum for different temperatures, Detector=InSb, polarization=//, resolution=0.03 cm^{-1}, aperture=1.7 mm, BS=CaF_2.

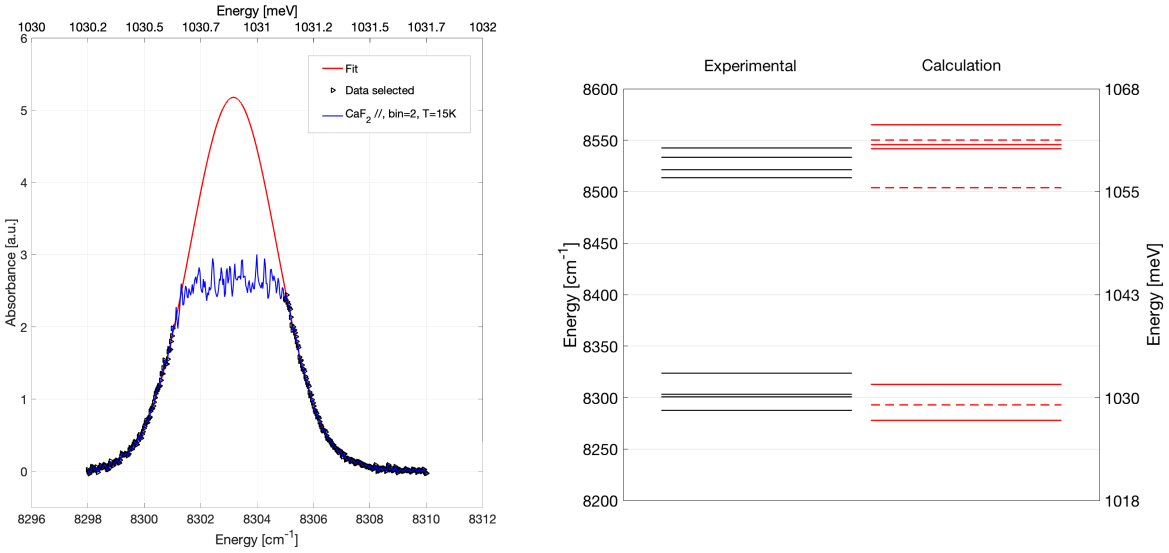

Figure 4.15 – Left: Voigt fit of a peak having a saturated signal, Detector=InSb, resolution=0.03 cm^{-1}, aperture=1.7 mm. Right: in red the calculated energy levels from Romanova [10] CF parameters. In dashed line the doublet state, in black the experimental results of this work.

State			Observed transitions			
Index	Energy [12] [cm^{-1}]	Symmetry	Initial State	Energy [cm^{-1}]	Pol.	Int. intensity [cm^{-1}]
$^3H_{5.1}$	8270	Γ_2	$^3H_{6.1}$	$(8287.25 \pm 0.06)^*$	x	(0.45 ± 0.42)
				$(8287.26 \pm 0.05)^*$	z	(1.94 ± 1.33)
$^3H_{5.2}$	8287	Γ_{34}	$^3H_{6.1}$	(8300.76 ± 0.07)	x	(0.58 ± 0.30)
				(8300.71 ± 0.07)	z	(0.39 ± 0.21)
$^3H_{5.3}$	8287	Γ_1	$^3H_{6.1}$	(8303.22 ± 0.06)	x	(6.72 ± 3.71)
				(8303.22 ± 0.06)	z	(7.16 ± 3.89)
$^3H_{5.4}$	8500	Γ_{34}	$^3H_{6.1}$	(8323.65 ± 0.05)	x	(0.58 ± 0.24)
				(8323.71 ± 0.08)	z	(0.20 ± 0.12)
$^3H_{5.5}$	8519	Γ_1	$^3H_{6.1}$	(8513.25 ± 0.29)	x	(1.39 ± 1.13)
				(8513.37 ± 0.08)	z	(7.79 ± 2.96)
$^3H_{5.6}$	-	Γ_2	$^3H_{6.1}$	(8521.73 ± 0.45)	x	(3.32 ± 1.87)
				(8521.16 ± 0.08)	z	(9.39 ± 3.69)
$^3H_{5.7a}$	-	Γ_{34}	$^3H_{6.1}$	(8531.47 ± 1.03)	x	(0.40 ± 0.23)
				(8527.32 ± 0.29)	z	(0.23 ± 0.13)
$^3H_{5.7b}$	-			(8534.44 ± 0.24)	x	(0.18 ± 0.11)
				(8531.04 ± 0.18)	z	(3.57 ± 2.01)
$^3H_{5.8}$	-	Γ_1	$^3H_{6.1}$	(8542.41 ± 0.04)	x	(7.66 ± 2.84)
				(8542.46 ± 0.12)	z	(1.63 ± 1.22)

Table 4.3 – Transition from the ground state to the $^3H_5$ manifold.
*the data at T=10K are used for the fit.

5 Conclusion and Perspectives

This work has presented the principle of the Fourier Transform Spectroscopy which was used to get the three first electronic excitation manifolds of the $LiTmF_4$ compound at cryogenic temperatures. Absorbance peaks from the first, second and third manifolds have been assigned to transitions from the ground state and the two first excited states.

For the far-infrared region some peaks are missing due to instrumental limitations and a too strong absorption from the sample. In the $^3F_4$ manifold, the first level observed at $5600\,\mathrm{cm}^{-1}$ is splitted in 6 resonances, while the second doubly degenerate states becomes two singlets due to crystal imperfection. By increasing the nominal temperature, one has been able to see transition arising from the first and second excited level instead of the ground state, which was initially hidden from the GS because of the selection rules, and therefore able to deduce the missing transition which matches the expecting values. The importance of Selection rules for electric and magnetic dipole has been then highlighted.

The unique high resolution and the brightness of this spectrometer have enable us to see a hyperfine splitting in the second manifold and its full origin remains unknown. The role of the selection rules has been highlighted, since there was a missing transition. However, knowing the energy difference between the ground state and the first excited as well as the emergence of new absorption peaks when increasing the temperature, leads to the deduction of the missing peak energy level. Furthermore, the numerical calculation are in very good agreement with the experimental results, since the relative difference is of the order of 0.1 %. However, while a doublet is numerically expected, two singlets are instead observed. As in the third manifold, the interpretation is the crystal imperfection, leading to lower the symmetry and a loss of degeneracy.

The transitions occurring in the $^3H_5$ manifold are the most complex to assign. Another other splitting appeared with an unknown origin. At the same time, two peak centers temperature dependent are identified and are attributed to the lattice vibration induced when heating. Finally, one transition remains untraceable and the selection rules might be the cause, since in that manifold the intensity transition depends strongly on the incident polarization beam. Nonetheless, new resonances that have not been measured before have been observed. The CF parameters which fit the best with our results are provided by Romanova study.

Further work needs to be done to unscramble all the transition and assign the type of transition. In particular, the low energy measurement was not completely satisfying since the second excited level could not be determinate accurately. In addition, the transmission signal was completely saturated. A thinner sample could solve this technical issue. The crystal studied is a pure $LiTmF_4$ compound, by doping one would be able to study deeper the absorption strength. Using the selection rules and polarization data we can in principle determine the nature of the transition.

It would have been great to retrieve the new set of CF parameters associated with the present work. *spectre* software provides the possibility to calculate the wave function for each state. We can use this information to directly find the relation between the experimental intensity and the calculated ones. Although, the numerical model does not take in account the hyperfine interaction which should be taken if the observation at $5600\,\mathrm{cm}^{-1}$ proves to be an hyperfine splitting, it is possible to include the Zeeman interaction. Therefore, applying an external magnetic field could lead to interesting comparisons. Finally, only the first 33 energy levels have been investigated. It will be worthwhile to reach the higher manifolds in order to get the most precise CF parameters and potentially discover new interesting features.

Acknowledgements

Firstly, I would like to thanks Prof. H. M. Rønnow and Peter Babkevitch from the LQM group who supervised me during the entire project. I am very grateful to every member of the PSI Quantum Technology group who helped me during the measurements. A special thank to Adrian Beckert from QT group for his scientific support and co-supervision. I thank Dr Arnaud Magrez who introduced me in magnetic research field and gave me nice advices.

My thanks go to my family and my dog Bambou who always supported me. Last but not least, thanks to my wonderful friends with whom I spent magical years, especially Aymeric Galan, Eric Paic, Etienne Droz and Nicolas Vallotton who were always present to do crazy things.

Thank you,

Lausanne, 6th July 2018 B. T.
revisited version, May 2020

A Units

Conversion Table of Energy and Wavelength Units

Wavenumber [cm^{-1}]	Wavelength [µm]	Wavelength [nm]	Frequency [GHz]	Electron Volt [eV]	Wavenumber [cm^{-1}]	Wavelength [µm]	Wavelength [nm]	Frequency [GHz]	Electron Volt [eV]
2.0	5 000.00	5 0000 00	60	.00 025	240.0	41.67	41 667	7 195	.02 976
4.0	2 500.00	2 500 000	120	.00 050	260.0	38.46	38 462	7 795	.03 224
6.0	1 666.67	1 666 667	180	.00 074	280.0	35.71	35 714	8 394	.03 472
8.0	1 250.00	1 250 000	240	.00 099	300.0	33.33	33 333	8 994	.03 720
10.0	1 000.00	1 000 000	300	.00 124	320.0	31.25	31 250	9 593	.03 967
12.0	833.33	833 333	360	.00 149	340.0	29.41	29 412	10 193	.04 215
14.0	714.29	714 286	420	.00 174	360.0	27.78	27 778	10 792	.04 463
16.0	625.00	625 000	480	.00 198	380.0	26.32	26 316	11 392	.04 711
18.0	555.56	555 556	540	.00 223	400.0	25.00	25 000	11 992	.04 959
20.0	500.00	500 000	600	.00 248	500.0	20.00	20 000	14 990	.06 199
22.0	454.55	454 545	660	.00 273	600.0	16.67	16 667	17 987	.07 439
24.0	416.57	416 667	719	.00 298	700.0	14.29	14 286	20 985	.08 679
26.0	384.62	384 615	779	.00 322	800.0	12.50	12 500	23 983	.09 919
28.0	357.14	357 143	839	.00 347	900.0	11.11	11 111	26 981	.11 159
30.0	333.33	333 333	898	.00 372	1 000.0	10.00	10 000	29 979	.12 398
32.0	312.50	312 500	959	.00 397	1 100.0	9.09	9 091	32 977	.13 638
34.0	294.12	294 118	1 019	.00 422	1 200.0	8.33	8 333	35 975	.14 878
36.0	277.78	277 778	1 079	.00 446	1 300.0	7.69	7 692	38 973	.16 118
38.0	263.16	263 158	1 139	.00 471	1 400.0	7.14	7 143	41 971	.17 358
40.0	250.00	250 000	1 199	.00 496	1 500.0	6.67	6 667	44 968	.18 598
50.0	200.00	200 000	1 499	.00 620	1 600.0	6.25	6 250	47 966	.19 837
60.0	166.67	166 667	1 799	.00 744	1 700.0	5.88	5 882	50 964	.21 077
70.0	142.86	142 857	2 099	.00 868	1 800.0	5.56	5 556	53 962	.22 317
80.0	125.00	125 000	2 398	.00 992	1 900.0	5.26	5 263	56 960	.23 557
90.0	111.11	111 111	2 698	.01 116	2 000.0	5.00	5 000	59 958	.24 797
100.0	100.00	100 000	2 988	.01 240	2 200.0	4.55	4 545	65 954	.27 276
110.0	90.91	90 909	3 298	.01 364	2 400.0	4.17	4 167	71 950	.29 756
120.0	83.33	83 333	3 597	.01 488	2 600.0	3.85	3 846	77 945	.32 236
130.0	76.92	76 923	3 897	.01 612	2 800.0	3.57	3 571	83 941	.34 716
140.0	71.43	71 429	4 197	.01 736	3 000.0	3.33	3 333	89 937	.37 195
150.0	66.67	66 667	4 497	.01 860	3 200.0	3.13	3 125	95 933	.39 675
160.0	62.50	62 500	4 797	.01 984	3 400.0	2.94	2 941	101 929	.42 155
170.0	58.85	58 824	5 096	.02 108	3 600.0	2.78	2 778	107 924	.44 634
180.0	55.56	55 556	5 396	.02 232	3 800.0	2.63	2 632	113 920	.47 114
190.0	52.63	52 632	5 696	.02 356	4 000.0	2.50	2 500	119 916	.49 594
200.0	50.00	50 000	5 996	.02 480	5 000.0	2.00	2 000	149 895	.61 992
220.0	45.45	45 455	6 595	.02 728	6 000.0	1.67	1 667	179 874	.74 390

Figure A.1 – taken from [21]

Bibliography

[1] P. E. Hansen, T. Johansson, and R. Nevald. Magnetic properties of lithium rare-earth fluorides: Ferromagnetism in $LiErF_4$ and $LiHoF_4$ and crystal-field parameters at the rare-earth and li sites. *Phys. Rev. B*, 12:5315–5324, Dec 1975.

[2] D. Bitko, T. F. Rosenbaum, and G. Aeppli. Quantum critical behavior for a model magnet. *Phys. Rev. Lett.*, 77:940–943, Jul 1996.

[3] Sushil K. Misra and Joshua Felsteiner. Low-temperature ordered states of lithium rare-earth tetrafluorides ($LiRF_4$). *Phys. Rev. B*, 15:4309–4312, May 1977.

[4] P. Babkevich, N. Nikseresht, I. Kovacevic, J. O. Piatek, B. Dalla Piazza, C. Kraemer, K. W. Krämer, K. Prokeš, S. Mat'aš, J. Jensen, and H. M. Rønnow. Phase diagram of diluted ising ferromagnet $LiHo_xY_{1-x}F_4$. *Phys. Rev. B*, 94:174443, Nov 2016.

[5] Conradin Kraemer, Neda Nikseresht, Julian O. Piatek, Nikolay Tsyrulin, Bastien Dalla Piazza, Klaus Kiefer, Bastian Klemke, Thomas F. Rosenbaum, Gabriel Aeppli, Ché Gannarelli, Karel Prokes, Andrey Podlesnyak, Thierry Strässle, Lukas Keller, Oksana Zaharko, Karl W. Krämer, and Henrik M. Rønnow. Dipolar antiferromagnetism and quantum criticality in $LiErF_4$. *Science*, 336(6087):1416–1419, 2012.

[6] D I Abubakirov, K Matsumoto, H Suzuki, and M S Tagirov. Anisotropic magnetization of the van vleck paramagnet $LiTmF_4$ at low temperatures and high magnetic fields. *Journal of Physics: Condensed Matter*, 20(39):395223, sep 2008.

[7] P. Babkevich, A. Finco, M. Jeong, B. Dalla Piazza, I. Kovacevic, G. Klughertz, K. W. Krämer, C. Kraemer, D. T. Adroja, E. Goremychkin, T. Unruh, T. Strässle, A. Di Lieto, J. Jensen, and H. M. Rønnow. Neutron spectroscopic study of crystal-field excitations and the effect of the crystal field on dipolar magnetism in $LiRF_4$ (R = Gd, Ho, Er, Tm, and Yb). *Phys. Rev. B*, 92:144422, Oct 2015.

[8] L. A. Bumagina, V. I. Krotov, B. Z. Malkin, and A. Kh. Khasanov. Magnetostriction in ionic rare earth paramagnets. *Sov. Phys. JETP*, 53:792–797, Apr 1981.

[9] G. Matmon, S. A. Lynch, T. F. Rosenbaum, A. J. Fisher, and G. Aeppli. Optical response from terahertz to visible light of electronuclear transitions in $LiYF_4$:Ho^{3+}. *Phys. Rev. B*, 94:205132, Nov 2016.

[10] I. V. Romanova, B. Z. Malkin, and M. S. Tagirov. Multipole interactions in a $LiTmF_4$ single crystal. *Optics and Spectroscopy*, 116(6):897–905, Jun 2014.

[11] W. T. Carnall, G. L. Goodman, K. Rajnak, and R. S. Rana. A systematic analysis of the spectra of the lanthanides doped into single crystal LaF_3. *The Journal of Chemical Physics*, 90(7):3443–3457, 1989.

[12] H. P. Christensen. Spectroscopic analysis of $LiTmF_4$. *Phys. Rev. B*, 19:6573–6582, Jun 1979.

[13] H. P. Jenssen, A. Linz, R. P. Leavitt, C. A. Morrison, and D. E. Wortman. Analysis of the optical spectrum of Tm^{3+} in $LiYF_4$. *Phys. Rev. B*, 11:92–101, Jan 1975.

[14] Binnemans K. Görller-Walrand C. *Handbook on the Physics and Chemistry of Rare Earths.* Springer, Berlin, Heidelberg, 1996.

[15] De Paula J. Atkins P. W. *Physical Chemistry.* Oxford University Press, 2002.

[16] Barbara H. Stuart. *Infrared Spectroscopy: Fondamentals and application.* John Wiley & Sons, 2004.

[17] Vij D.R. Jaggi N. *Fourrier Transform Infrared Spectroscopy.* Springer,Boston,MA, 2006.

[18] Chantry G. W. Stone N. W. B. Chamberlain, J. E. *The Principles of Interferometric Spectroscopy.* Chichester, 1979.

[19] Marcel Snels, Veronika Horká-Zelenková, Hans Hollenstein, and Martin Quack. *High-Resolution FTIR and Diode Laser Spectroscopy of Supersonic Jets.* American Cancer Society, 2011.

[20] Lawrence Mertz. *Transformations in Optics.* John Wiley & Sons, 1965.

[21] Bruker Optics. *Guide for Infrared Spectroscopy.* 2009.

[22] Winefordner J. D. Griffiths P. R., De Haseth J. A. *Fourier Transform Infrared Spectroscoy.* 2 edition, 2007.

[23] Walter S. Struve. *Fundamentals of Molecular Spectroscopy.* Wiley, 1989.

[24] Olivero J. J. and Longbothum R. L. Empirical fits to the voigt line width: a brief review. *J. Quant. Spectrosc. Radiat. Transfer*, 17:233–236, 1977.